



A Comparison of Star-forming Clumps and Tidal Tails in Local Mergers and High-redshift Galaxies

Debra Meloy Elmegreen¹, Bruce G. Elmegreen², Bradley C. Whitmore³, Rupali Chandar⁴, Daniela Calzetti⁵, Janice C. Lee⁶, Richard White³, David Cook⁶, Leonardo Ubeda³, Angus Mok⁴, and Sean T. Linden⁵

¹ Department of Physics & Astronomy, Vassar College, Poughkeepsie, NY 12604, USA; elmegreen@vassar.edu

² IBM Research Division, T.J. Watson Research Center, 1101 Kitchawan Road, Yorktown Heights, NY 10598, USA

³ Space Telescope Science Institute, 3700 San Martin Drive, Baltimore, MD 21218, USA

⁴ Department of Physics & Astronomy, University of Toledo, Toledo, OH 43606, USA

⁵ Dept. of Astronomy, University of Massachusetts at Amherst, Amherst, MA 01003, USA

⁶ Infrared Processing and Analysis Center (IPAC), California Institute of Technology, Pasadena, CA 91125, USA

Received 2020 October 12; revised 2020 December 5; accepted 2020 December 18; published 2021 February 18

Abstract

The Clusters, Clumps, Dust, and Gas in Extreme Star-forming Galaxies (CCDG) survey with the Hubble Space Telescope includes multiwavelength imaging of 13 galaxies less than 100 Mpc away, spanning a range of morphologies and sizes, from blue compact dwarfs to luminous infrared galaxies, all with star formation rates in excess of hundreds of solar masses per year. Images of seven merging galaxies in the CCDG survey were artificially redshifted to compare with galaxies at $z = 0.5$, 1, and 2. Most redshifted tails have surface brightnesses that would be visible at $z = 0.5$ or 1 but not at $z = 2$ due to cosmological dimming. Giant star clumps are apparent in these galaxies; the 51 measured have similar sizes, masses, and colors to clumps in observed high- z systems in the UDF, GEMS, GOODS, and CANDELS surveys. These results suggest that some clumpy high- z galaxies without observable tidal features could be the result of mergers. The local clumps also have the same star formation rate per unit area and stellar surface density as clumps observed at intermediate and high redshift, so they provide insight into the substructure of distant clumps. A total of 1596 star clusters brighter than $M_V = -9$ were identified within the boundaries of the local clumps. The cluster magnitude distribution function is a power law with approximately the same slope (~ -1 for a plot of number versus log luminosity) for all the galaxies both inside and outside the clumps and independently of clump surface brightness.

Unified Astronomy Thesaurus concepts: Galaxy evolution (594); High-redshift galaxies (734); Interacting galaxies (802); Starburst galaxies (1570)

1. Introduction

Star formation in galaxies in the early universe was driven by a combination of cold flows (see review in Sancisi et al. 2008; Sánchez Almeida et al. 2014) and mergers (see review in Conselice 2014). Simulations such as EAGLE (Schaye et al. 2015), IllustrisTNG (Pillepich et al. 2018), and SIMBA (Davé et al. 2019) show both processes and reproduce the observed atomic and molecular gas properties well (Davé et al. 2020).

Disk galaxies are increasingly clumpy and irregular at high redshift (e.g., Cowie et al. 1995; van den Bergh et al. 1996; Elmegreen & Elmegreen 2005; Elmegreen et al. 2007a, 2007b; Guo et al. 2018), and the gas velocity dispersions are several times higher than in local disk galaxies (e.g., Tacconi et al. 2010; Wisnioski et al. 2015, 2019; Simons et al. 2017). Star-forming clumps (often referred to in local galaxies as “complexes” or “star-forming complexes;” “clumps” will be used throughout this paper) of kiloparsec size can be resolved out to redshifts $z = 4\text{--}5$ (Elmegreen & Elmegreen 2005; Elmegreen et al. 2007a, 2007b, 2009b; Guo et al. 2015, 2018), but their substructure is not resolved. While clumps in local galaxies can be resolved into clusters, clumps in local isolated galaxies are much less massive (by $100\times$ or more) than those at high redshift (which are typically $10^8\text{--}10^9 M_\odot$) since they formed under more quiescent conditions (Elmegreen et al. 2009b). Local dwarf irregular galaxies are low-mass analogs of high-redshift clumpy galaxies, although they evolve more slowly and with lower star formation rates (Elmegreen et al. 2009a).

Local merging or strongly interacting galaxies, on the other hand, show extreme star formation not seen in isolated galaxies, including massive star clusters in the Antennae (Whitmore et al. 2010) and other luminous infrared galaxies (LIRGS; Linden et al. 2017; Adamo et al. 2020). Zaragoza-Cardiell et al. (2018) examined over 1000 clumps in 46 nearby interacting galaxies and nearly 700 clumps in 38 non-interacting spirals to compare their large-scale properties. From multiwavelength spectral energy distribution fits for the identified clumps, they found that the star formation rates per unit area are higher and the clumps tend to be younger in the interacting than in the non-interacting galaxies. Larson et al. (2020) studied 810 clumps in 48 local LIRGS from narrowband Hubble Space Telescope (HST) imaging and found that the sizes and star formation rates span a broad range between that seen in local quiescent galaxies and that found in $z = 1\text{--}3$ galaxies, with the largest (kiloparsec size) clumps resembling those in the high- z galaxies. Note that Cava et al. (2017) analyzed a clumpy high-redshift galaxy with multiple gravitationally lensed images, and found that clumps are smaller (by a factor of 2–3 on average) when viewed with higher magnification. Thus, clumps with sizes from a few hundred parsecs to about a kiloparsec in nearby galaxies are appropriate for comparison with high- z clumps. If clumps in local mergers have photometric properties similar to those in high- z galaxies, then local clumps can provide insight into the substructure of clumps not resolved at high z .

We are also interested in the appearance of major mergers at high redshift and whether some distant clumpy galaxies

without the usual tidal features can be hidden mergers. Mergers might be expected to have distinguishing characteristics such as asymmetry, tidal tails, multiple nuclei, and complex kinematics. However, at high redshift these can be difficult to recognize (Hopkins et al. 2010). For example, simulations by Hung et al. (2016) and Simons et al. (2019) found that line-of-sight velocity distributions inside major mergers at $z \sim 2$ can resemble those in isolated disks. Blumenthal et al. (2020) suggested that visual classifications of mergers have a bias toward massive galaxies in dense environments where tidal effects are large and surface brightnesses are high; they identified only half of the mergers in mock catalogs made from the IllustrisTNG-100 simulation.

Nevertheless, several studies have found the merger fraction as a function of redshift using various combinations of features. Xu et al. (2020) found, on the basis of asymmetry, color, and comparisons to the Illustris simulation, that for high-mass galaxies, $>10^{11.3} M_{\odot}$, at redshift $z \sim 0.5$, 20% are star-forming, and 85% of those are mergers. Duncan et al. (2019) measured pair counts at 5–30 kpc separation and found that the comoving major merger rate was constant to $z = 6$ at masses greater than $10^{10.3} M_{\odot}$ and that the growth of these galaxies by mergers was comparable to the growth by star formation at $z > 3$. O’Leary et al. (2021) showed that major mergers are more frequent at high mass ($10^{11} M_{\odot}$) and low redshift, where they can dominate the mass growth of these galaxies over in situ star formation by up to a factor of ~ 10 . Ventou et al. (2019) combined separation and velocity information for mergers in Illustris and compared that to MUSE data in several deep fields, concluding that 25% of close pairs with mass greater than $10^{9.5} M_{\odot}$ are major mergers at redshifts of 2–3, with a decreasing fraction beyond this. Ferreira et al. (2020) used Bayesian deep learning models applied to large galaxy samples and simulations to suggest that the fraction of mergers may be $\sim 3\%$ at $z = 0.5$, increasing to $\sim 7\%$ at $z = 1$ and $\sim 22\%$ at $z = 2$.

Other methods have been used to identify mergers also. Ribeiro et al. (2017) looked at ~ 1200 galaxies at $z = 2$ –6 and found that most of the clumpy galaxies have only two clumps. They also noted that these two-clump galaxies have the biggest clumps. They then derived a major merger fraction of 20% by considering that the large clumps are merging galaxies and the small clumps are in situ star formation. Zanella et al. (2019) also considered clumps of extended emission or what they refer to as “blobs” around clumpy galaxies at $z = 1$ –3 and proposed that peripheral blobs are companions while compact blobs are in situ star formation. The galaxy merger fraction in their sample was less than 30% for typical mass ratios of 1:5.

Tidal tails are another indication of mergers. Wen & Zheng (2016) studied long tidal tails in the COSMOS field, and when compared to galaxy pairs they suggested that around half of disk galaxy mergers at $z < 1$ produce detectable tails. An early catalog of 100 galaxies out to $z \sim 1.4$ with various types of tidal features was given by Elmegreen et al. (2007a); the disks and tidal tails in that study were about a factor of 2 smaller than local disks and tails. This smaller size is consistent with the observation of shorter merger times at high redshift (e.g., Snyder et al. 2017; Mantha et al. 2018). Elmegreen & Elmegreen (2006) also cataloged ring galaxies and curved chain galaxies that could be signs of interactions. These studies indicate that mergers out to $z \simeq 1$ often show observable signs of the interaction. At higher redshifts, tidal features become difficult to observe.

Another reason why major mergers are difficult to recognize at high redshift is that they rarely trigger a large excess of star formation. Most nearby mergers do not have a large excess in star formation rate either (Knapen et al. 2015), which is unlike local ULIRGS, which are late-stage mergers and do trigger significant star formation (e.g., Sanders & Mirabel 1996; Tacconi et al. 2002). For high redshift, Martin et al. (2017) used cosmological simulations to show that even with major and minor mergers, most star formation in a galaxy is in situ, with only 35% at $z \sim 3$ and 20% at $z \sim 1$ from enhancements during a merger. Similarly, Mundy et al. (2017) studied a sample of mass-selected galaxy pairs and found that star formation during major mergers represents only 1%–10% of the stellar mass growth at high z . Fensch et al. (2017) used parsec-resolution hydrodynamical simulations to compare star formation rates in merging gas-rich galaxies. They showed that high-redshift mergers have smaller excess star formation rates than low-redshift mergers by about a factor of 10 because of the generally high velocity dispersion and instability level in high-redshift galaxies even without a merger. Pearson et al. (2019) used convolutional neural networks to identify binary mergers in the Sloan Digital Sky Survey, Kilo Degree Survey, and Cosmic Assembly Near-infrared Deep Extragalactic Legacy Survey (CANDELS). They examined excess star formation rates above the galaxy main sequence and found only a factor of 1.2 more star formation for merging galaxies. Wilson et al. (2019) studied 30 galaxy pairs within 60 kpc and 500 km s^{-1} of each other at redshifts of 1.5–3.5 (12 were major mergers) and found no significant enhancement in star formation rate.

Among galaxies with excessive star formation rates (i.e., significantly above the star formation main sequence), however, most are major mergers. Cibinel et al. (2019) studied close pairs and morphological mergers on and above the star formation main sequence up to $z = 2$ and found a merger fraction greater than 70% above the main sequence, although as in the other studies, the morphological mergers on the main sequence did not have much excess star formation.

In this paper, we examine the properties of large-scale star-forming clumps and tidal tails in seven nearby major mergers in the HST Clusters, Clumps, Dust, and Gas in Extreme Star-forming Galaxies (CCDG) survey. We measure the clump photometric properties for comparison with previously observed high- z clumps. We further consider whether high- z clumps might contain massive star clusters that are not directly visible in most surveys, using HST observations of the local mergers to identify star clusters inside their clumps. By artificially redshifting the local mergers to mimic their appearance at $z = 0.5$, 1, and 2, we consider whether the comparatively poor angular resolution and surface brightness dimming at high redshift make major mergers resemble isolated clumpy galaxies.

Section 2 presents the data used in this study, Section 3 describes how the images are artificially redshifted to compare with previous observations of galaxies in samples at moderate to high redshift, Section 4 presents the photometry for clumps and compares it with properties of clumps in high-redshift galaxies, and Section 5 considers the star clusters within each clump. Section 6 discusses the tidal tail features in local and distant systems, Section 7 discusses extinction effects and gas properties, and Section 8 summarizes our conclusions.

Table 1
Galaxies

Name	F275W Camera	F336W Camera	F435W Camera	F438W Camera	F555W Camera	F814W Camera	Distance (Mpc)	Scale (pc px ⁻¹)	No. Clumps	No. Clusters (in Clumps)
Arp 220	WFC3	WFC3	ACS	...	WFC3	ACS	81.5	15.6	9	28
ESO 185–IG13	WFC3	WFC3	WFC3	WFC3	81.6	15.6	4	81
Haro 11	WFC3	...	ACS	...	WFC3	WFC3	90.8	17.4	3	65
NGC 1614	WFC3	WFC3	ACS	...	WFC3	ACS	69.2	13.2	13	72
NGC 2623	WFC3	...	ACS	...	ACS	ACS	80.9	15.5	13	116
NGC 3256	WFC3	WFC3	ACS	...	ACS	ACS	38.1	7.3	4	406
NGC 3690	WFC3	WFC3	ACS	WFC3	WFC3	ACS	47.3	9.1	5	828

Note. Distance is the Galactocentric Standard of Rest distance from the NASA/IPAC Extragalactic Database (NED; <https://ned.ipac.caltech.edu/>).

2. Data

The HST survey of CCDG by R. Chandar et al. (2021, in preparation) includes 13 extreme star-forming galaxies in the nearby universe. For this paper, we used multiwavelength observations of seven merging or strongly interacting systems in the survey: Arp 220, ESO 185–IG13, Haro 11 (ESO 350–IG038), NGC 1614, NGC 2623, NGC 3256, and NGC 3690. Arp 220 is an ultraluminous infrared galaxy (ULIRG), NGC 1614, NGC 2623, NGC 3256, and NGC 3690 (Arp 299) are LIRGS, and ESO 185–IG13 and Haro 11 are blue compact galaxies. Their distances range from 38 to 90 Mpc. Photometry was done on images observed with HST Advanced Camera for Surveys (ACS) or WFC3 using the filters F275W, F336W, F435W, F438W, F555W, and F814W. (Images were also obtained with filters F110W, F130N, and F160W, although they are not used in this paper.) The images were drizzled and aligned, with a pixel scale of 0".0396. Table 1 lists the galaxies, the filters and cameras used in this study, distances, and linear scales, along with the number of clumps and number of clusters within clumps.

3. High-redshift Appearance

Following the procedure of Elmegreen et al. (2009b), we have Gauss-blurred the HST images to the spatial resolution a galaxy would have at redshifts $z = 0.5$, 1, and 2. Next the images were re-pixelated to mimic how they would appear at a higher z . Finally, noise was added to account for cosmological dimming, which reduces the intensity by $(1+z)^4$.

The Gauss blurring was done as follows. The spatial size of 1 pixel was determined for redshifts $z = 0.5$, 1, and 2, which corresponds to 240 pc, 318 pc, and 335 pc, respectively, using the standard cosmological model (Hubble constant parameter $h = 0.72$; Spergel et al. 2003). The FWHM of a point source is $F = 2.05$ px, based on Legacy ExtraGalactic UV Survey (LEGUS) measurements for HST images. The product of these two quantities gives the number of pc in a FWHM for the redshifted version of the galaxy. This product is divided by the number of parsecs in a pixel for the local galaxy to give the number of pixels, S , in the local galaxy that corresponds to the size of a FWHM in the redshifted version. Then the Gauss blur factor, G , was $G = \sqrt{S^2 - F^2}$. The corresponding Gaussian σ for the blur is $G/(8 \ln 2)$, used in the IRAF task Gauss. Next, we re-pixelated the images with the IRAF task *blkavg*, setting the block average to be the ratio S/F . Finally, we measured the sky rms in the original image and added noise to the blurred, re-pixelated image to give it the same ratio of peak intensity to

sky rms as in the original image, using the IRAF task *mknoise*. The output of these steps is an image of the galaxy with the same physical resolution, pixelation, and noise level as the galaxy would show at each redshift.

The results are shown in Figures 1–4 for each galaxy for the F435W (or F438W) images and in Figures 5–7 for the F275W images. The F275W image was very faint for Arp 220 so is not included.

Images in these two filters were selected for ease in comparison with other observations: the F275W artificially redshifted images are appropriate for comparison with a $z = 2$ galaxy observed in the R band, a $z = 1$ galaxy observed in the B band, or a $z = 0.5$ galaxy observed in the U band, while the F435W artificially redshifted images are appropriate for comparison with J -band, I -band, and R -band images for galaxies at $z = 2$, 1, and 0.5, respectively.

Merging galaxies out to $z \sim 1$ studied by Elmegreen et al. (2009b) in the Great Observatories Origins Deep Survey (GOODS; Giavalisco et al. 2004) and Galaxy Evolution from Morphology and SEDs (GEMS; Rix et al. 2004) fields also contained clumps. The classified morphologies were “diffuse,” which have indistinct tidal patches or shells of modest size, “antennae,” which have two main tidal arms, “M51-type,” which have a long tidal arm pointing to a companion, and “shrimp-like,” which have one long and curved clumpy arm connected to a head of about the same width. The seven galaxies in the current sample most resemble the diffuse and antennae morphologies: NGC 2623 is antennae-like, while the other six are diffuse.

Some bright galaxies, like Arp 220, have tidal features that would still be apparent at higher z , although for most galaxies only the bright centers would be evident. Haro 11, for example, has the appearance of a clumpy galaxy at higher z ; NGC 2623 would just be a double galaxy at $z = 2$. Several of the galaxies still show some tidal arms at $z = 1$. The tail surface brightnesses and clump properties will be compared with high-redshift interacting galaxies in more detail below.

4. Clump Properties

4.1. Clump Photometry

Clumps are identified as extended dense regions. Since clumps are hierarchical, they subdivide into smaller star-forming regions with higher resolution. In order to compare clumps in our galaxies with those in high-redshift galaxies, we identified clumps by visual inspection of the $z = 2$ images in the F435W band.

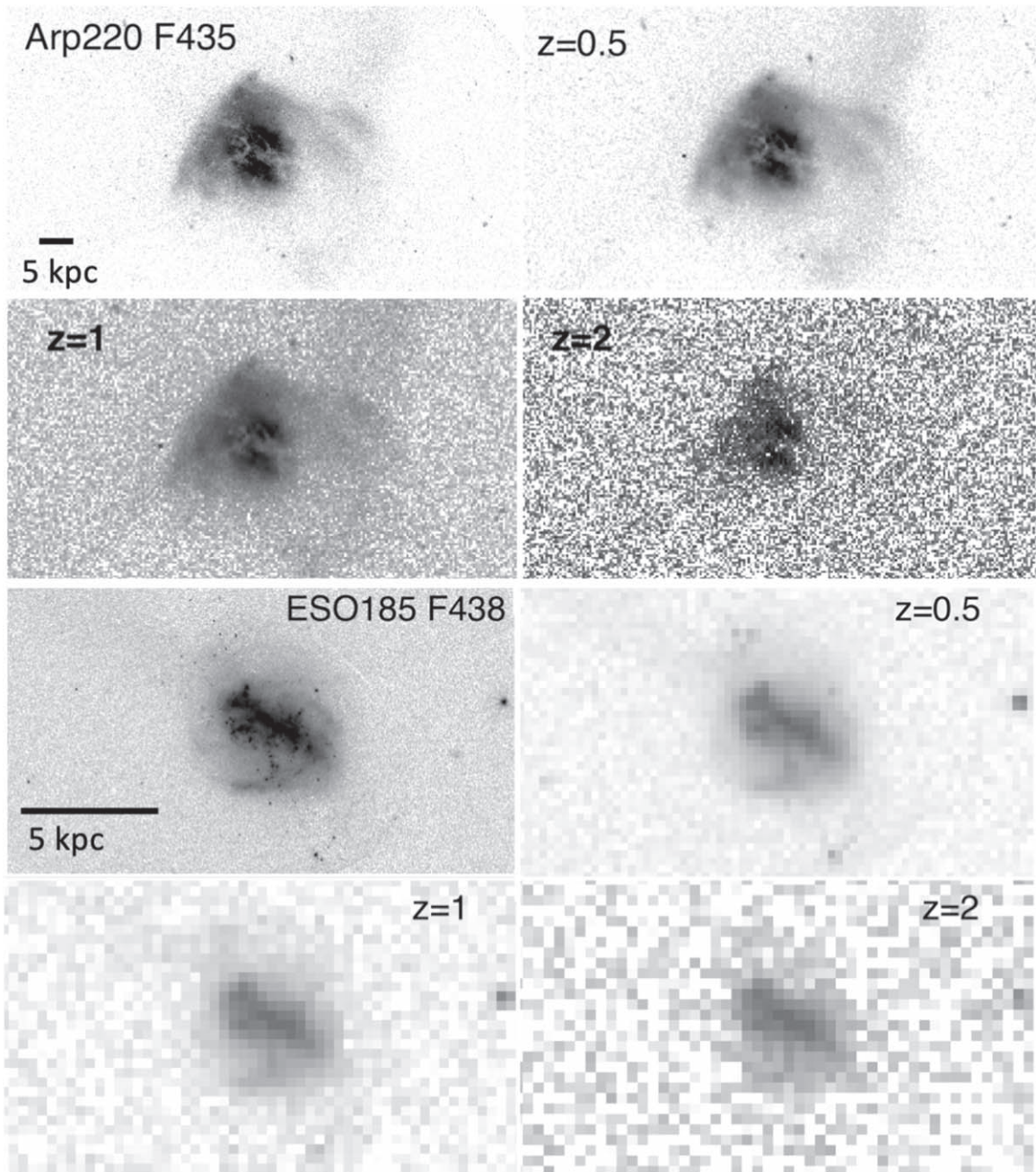


Figure 1. Arp 220 and ESO 185 are shown in filter F435W, and artificially redshifted to $z = 0.5$, 1, and 2 in the panels, as labeled. The spatial size of 1 pixel for redshifts $z = 0.5$, 1, and 2 corresponds to 240 pc, 318 pc, and 335 pc, respectively; the pixel scale of the rest-frame image for each galaxy is given in Table 1. Black lines indicate a physical scale of 5 kpc. The F435 artificially redshifted image is appropriate for comparison with images in the J band, R band, and I band for galaxies at $z = 2$, 1, and 0.5.

Measurements were made on the original non-redshifted images since the simulated redshifted images were Gauss-blurred and re-pixelated with artificial noise added, so flux would have been difficult to determine accurately. Instead, contour plots were made on the local images and compared with the $z = 2$ images where the clumps were distinct. In practice, the contours at $10 \times \text{sky } \sigma$ on the local images matched the clumps in the high- z images, so that is where the boxes were defined for photometry. The IRAF task *imstat* was used to determine total pixels and mean counts per pixel within the boxes. Magnitudes were then determined for each clump, using the zero-points from the WFC3 and ACS handbooks. There was no background subtraction, because the photometric

fitting described below included an underlying component plus the star-forming component, described further below. This is the same procedure as we used in measuring clumps in high-redshift galaxies (Elmegreen et al. 2009b), so our results for clumps in our galaxies can be directly compared to the high-redshift results. For the galaxies in this paper, this means the clump boundaries sometimes contain more than one large clump, since some get blended at high z .

The measured clumps are indicated as boxes in Figure 8. For Haro 11, contour plots are also shown as an example of how clumps were identified. The right-hand contour plot is on the simulated $z = 2$ F435W image, where the three clumps are distinct. The middle contour plot on the original image has an

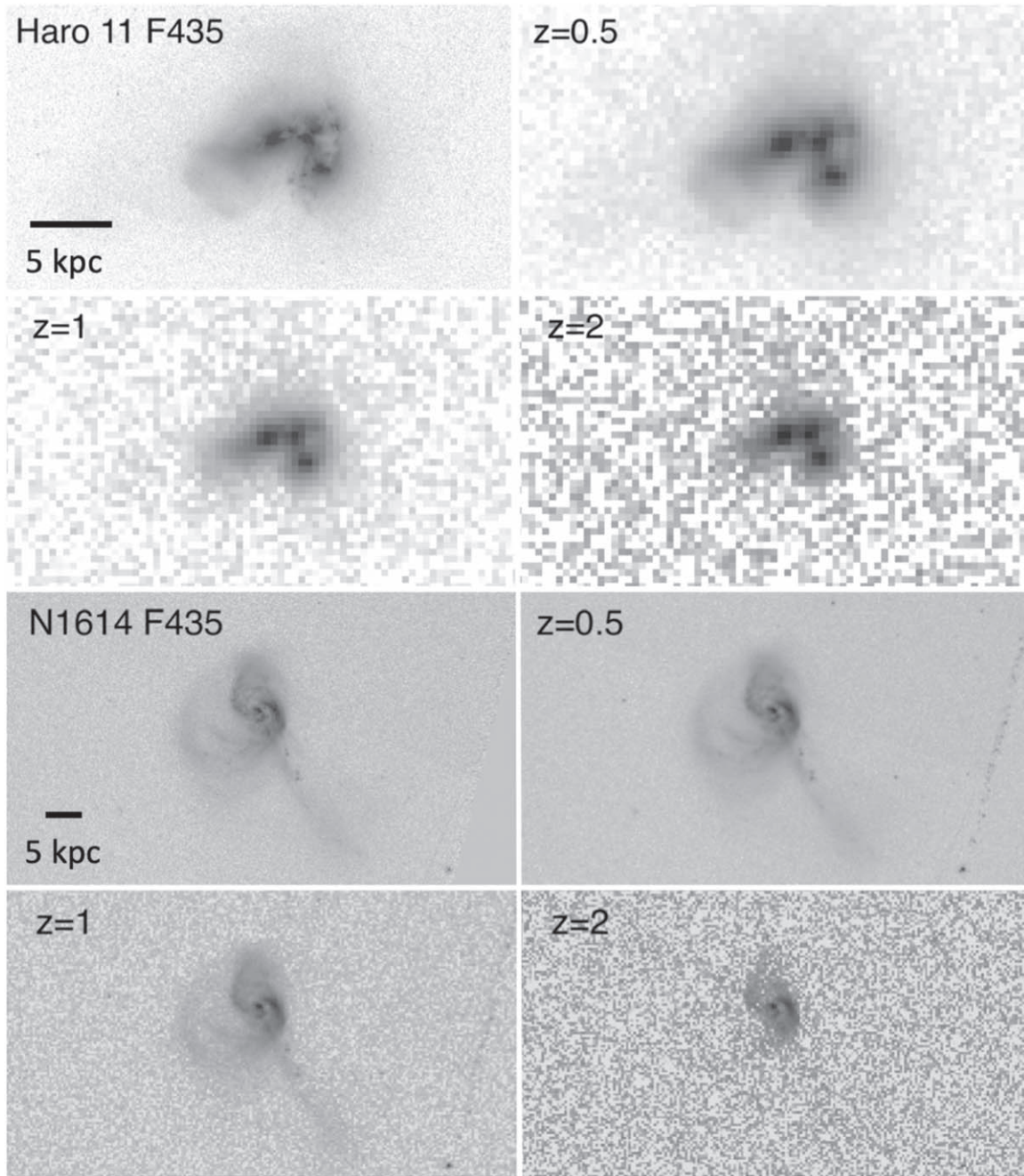


Figure 2. Haro 11 and NGC 1614 are shown in filter F435W, and artificially redshifted to $z = 0.5$, 1, and 2 in the panels, as labeled. Black lines indicate a physical scale of 5 kpc.

arrow indicating the $\sim 10 \times$ sky σ contour where the boxes were then drawn. A total of 51 clumps were identified in the seven galaxies (the number in each galaxy is listed in Table 1). The average absolute B -band magnitude of the clumps for the seven galaxies in this sample is -15.4 ± 2.6 , while the average $(B - V)$ color is 0.4 ± 0.5 . The clump diameters are approximated by the square root of the area of the boxes defined for photometry, and range from 170 pc to 2.9 kpc, with an average of 1.0 ± 0.7 kpc.

4.2. Clump Ages and Masses

The photometric measurements of the clumps were used to determine ages, masses, and extinctions through spectral

energy distribution (SED) fitting, as detailed in Elmegreen et al. (2009a). The procedure multiplied the throughput of each HST filter by an integrated spectrum using stellar population models from Bruzual & Charlot (2003) with a Chabrier initial mass function and solar metallicity. The integrated spectrum contained two components: a constant star formation rate for the full span of time in Bruzual & Charlot (2003) representing the underlying galaxy, plus another constant rate for some variable time representing burst star formation in the clump.

The ratio of the burst rate to the underlying rate ranged from 10 to 10^4 in 12 logarithmic steps, the start time for the burst ranged from 10^7 to 10^9 yr in eight logarithmic steps, and the visual extinction ranged from 0 to 10 mag in steps of 0.1 mag. For each combination of parameters, the colors of the

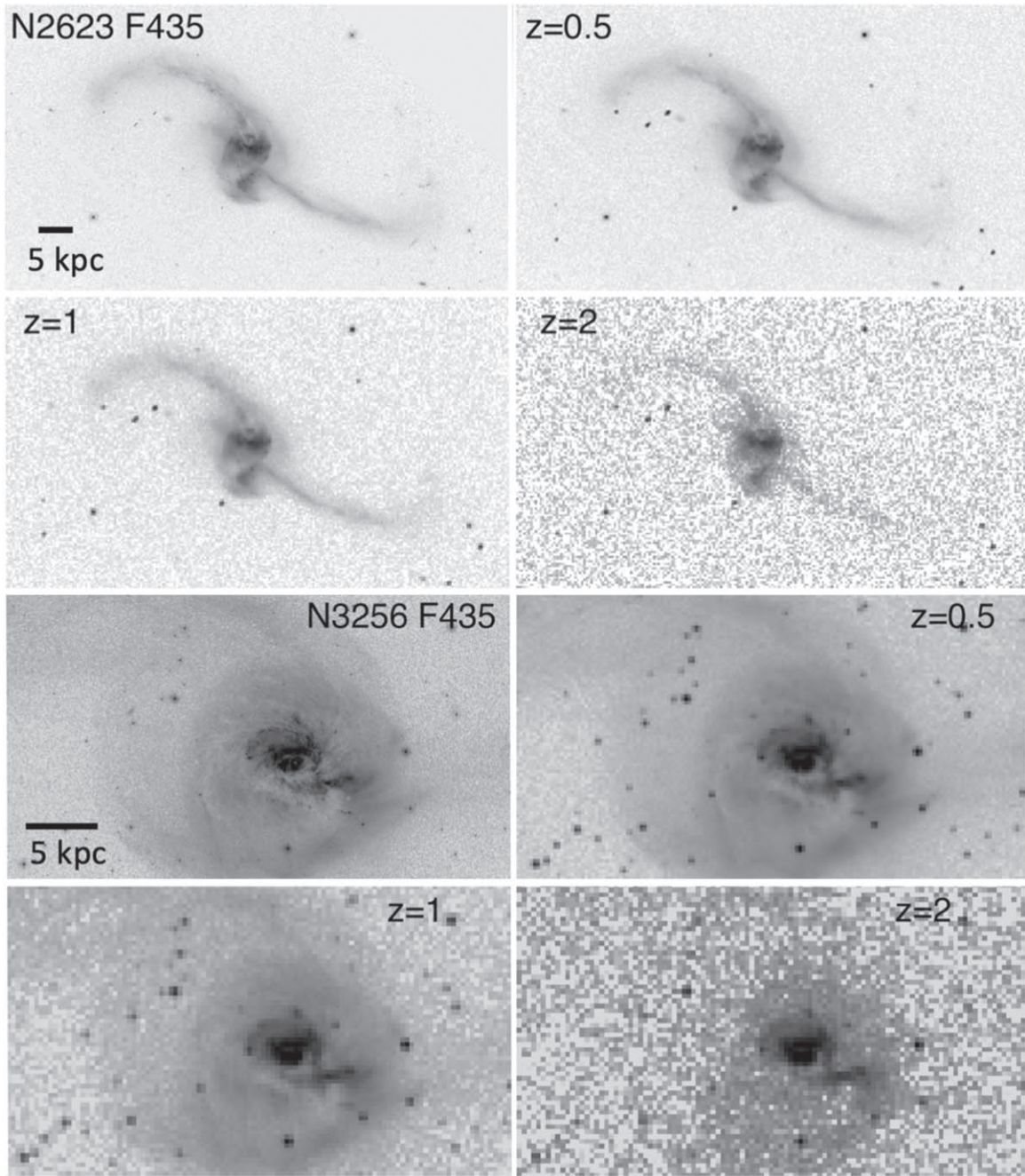


Figure 3. NGC 2623 and NGC 3256 are shown in filter F435W, and artificially redshifted to $z = 0.5, 1$, and 2 in the panels, as labeled. Black lines indicate a physical scale of 5 kpc.

integrated spectrum were differenced from the observed clump colors and divided by the measurement error in that color, and the sum of the squares of these normalized differences was determined. This sum is considered to be the χ^2 value of the fit. The best fit parameters were then taken to be the weighted average of the input parameters with a weighting factor equal to $\exp(-w\chi^2)$, where w is a parameter chosen to make the weighting factors vary slowly around the maximum weight. The measurement error for color was taken to be the square root of the sum of the squares of the measurement errors for each passband, and the latter were taken to be the ratio of the standard deviation of the flux count to the flux itself, averaged for all pixels in the clump (from IRAF *imstat*) divided by the square root of the number of pixels in the clump. The

measurement errors are generally much lower than the color differences among the models, so w was chosen to be fairly large to keep the exponential weighting factor close to unity; we choose $w = 2^{0.5} \times 20$ after some experimentation. The model uncertainty was determined from the range of model values with the lowest χ^2 .

These models do not alone give the clump masses or star formation rates, because they fit only the star clump colors. The evaluation of mass and absolute magnitude in each passband comes from a comparison between the observed and model I -band fluxes. That is, the absolute mass was obtained from the product of the model mass and the ratio of the observed I -band flux to the model I -band flux. (The results for mass in what follows refer to the mass of the young component in the

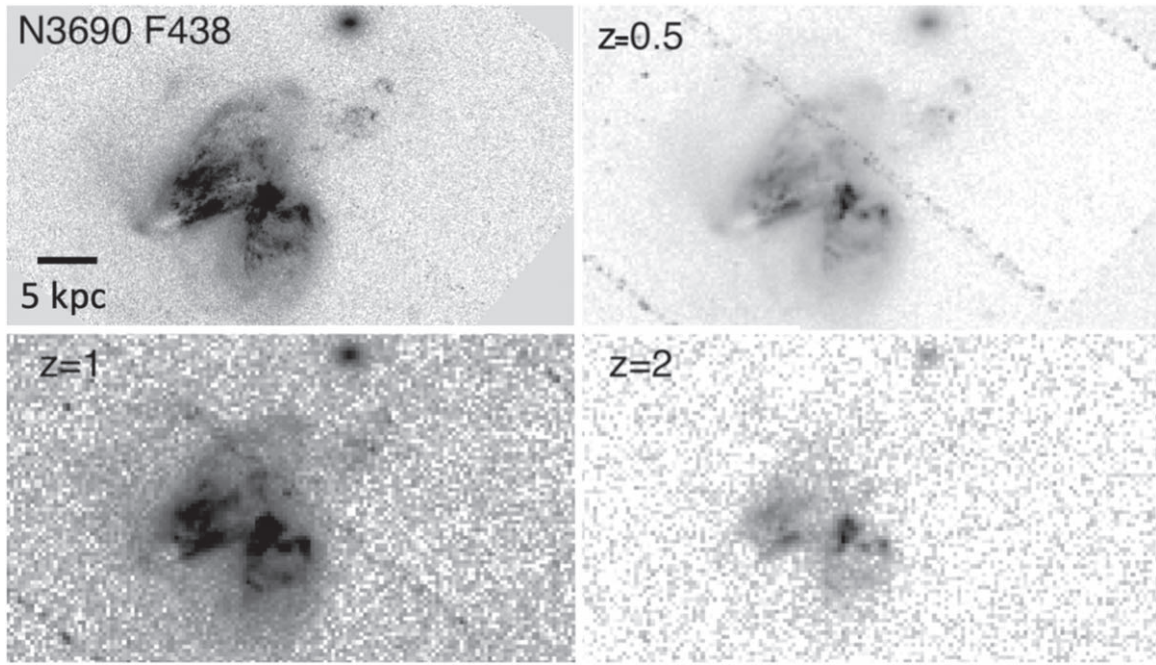


Figure 4. NGC 3690 is shown in filter F438W in the upper left panel, and artificially redshifted to $z = 0.5, 1$, and 2 in the panels, as labeled. The black line indicates a physical scale of 5 kpc.

two-component population fit for a clump, unless otherwise indicated.) Because of a general ambiguity in stellar population colors between age and extinction, and a compensation between these ambiguities in the determination of mass, the fitted masses are considered to be more accurate than the ages and extinctions. The average error in the fits was 0.13 in log mass, 0.33 in log age, and 0.27 in A_V .

Figure 9 shows sample fits for three galaxies. Red crosses represent the photometric measurements and blue dots with uncertainties are the models. Results are plotted in AB magnitudes since those were used in the SEDs.

The average mass, age, and extinction A_V of the clumps within each galaxy are tabulated in Table 2, and histograms of mass, age, and extinction are shown in Figure 10. We omitted seven poorly fit clumps (three in Arp 220, four in NGC 2623) from the averages and histograms because their mean squared difference between the observed and modeled colors was greater than 1 (in units of mag^2). The left-hand panel of Figure 10 shows a histogram of the young stellar masses in all the clumps (i.e., not including the underlying component, which would add approximately a factor of 2 to the clump mass). The log masses in M_\odot range from 5.2 to 9.6, with an average of 7.6 ± 1.2 . The largest clumps are probably the nuclei of the merging galaxies. For example, the most massive clump, which is in the center of Arp 220, has a dynamical mass of $1.5 \times 10^9 M_\odot$ (Wheeler et al. 2020).

As a check on some individual derived masses, we note that MUSE Very Large Telescope (VLT) $H\alpha$ observations of Haro 11 yield a dynamical mass of $\sim 10^8 M_\odot$ for the largest clump (Menacho et al. 2019), compared with our value of $8.15 \times 10^7 M_\odot$. For the other two clumps, Adamo et al. (2010) derive masses of $8.35 \times 10^6 M_\odot$ and $1.36 \times 10^7 M_\odot$ based on point-source photometry of HST observations at the peak brightness, compared with our estimates of $7.76 \times 10^7 M_\odot$ and $2.29 \times 10^7 M_\odot$, respectively. Our clump boundaries are much larger than those in Adamo et al. (2010) since we defined the extended

clumps rather than the peak sources. We derived slightly older estimated ages since the boundaries extended beyond the brightest star-forming site, but similar extinctions (ours was $1.0 A_V$ mag compared with their $1.2 A_V$ mag for their Knot B).

Our derived log ages in years (shown in the middle panel of Figure 10) range from 7.3 to 9, with an average 8.4 ± 0.6 . The fitted extinctions in the V band (shown in the right panel of the figure) range from 0.2 to 4.2 mag (for a dusty central region in Arp 220), with an average of 1.6 ± 1.0 . Arp 220 and NGC 2623 have the oldest clumps.

The clumps encompass extreme star formation. As an approximate measure of the average clump star formation rate (SFR) in $M_\odot \text{ yr}^{-1}$, we take the young stellar clump mass divided by the age. Then the star formation rate per unit area, Σ_{SFR} in $M_\odot \text{ yr}^{-1} \text{ kpc}^{-2}$, is given by the SFR divided by the area of the clump converted to square kiloparsecs using the values in Table 1. Table 2 lists the average $\log(\text{SFR})$, and the log of the specific star formation rate (sSFR), taken to be the SFR divided by the total mass in the clump, including the underlying component plus the new star formation.

A plot of Σ_{SFR} versus SFR is shown in Figure 11. The black dots represent the clumps measured here, and the red dots represent the whole galaxies (Chandar 2018). The galaxies fall in the realm of other LIRGs. For a given SFR, the value of Σ_{SFR} is about $25\times$ higher for the clumps than for each galaxy as a whole. $\log(\text{sSFR})$ ranges from -9.0 to -7.6 , with an average of -8.7 ± 0.4 ; average sSFRs for clumps within each galaxy are listed in Table 2. These values are similar to those for the ULIRGs in Vivian et al. (2012, Table 11), which have an sSFR for the whole galaxy ranging from -8.9 to -10.0 , with an average of -9.1 ± 0.4 . The logarithms of the surface densities of the clumps in our sample in $M_\odot \text{ pc}^{-2}$ average 1.97 ± 0.72 (averages in each galaxy are in Table 2), so are about $100 M_\odot \text{ pc}^{-2}$.

The clump age as a function of Σ_{SFR} is shown in the left panel of Figure 12, along with the curve fit. There a very weak

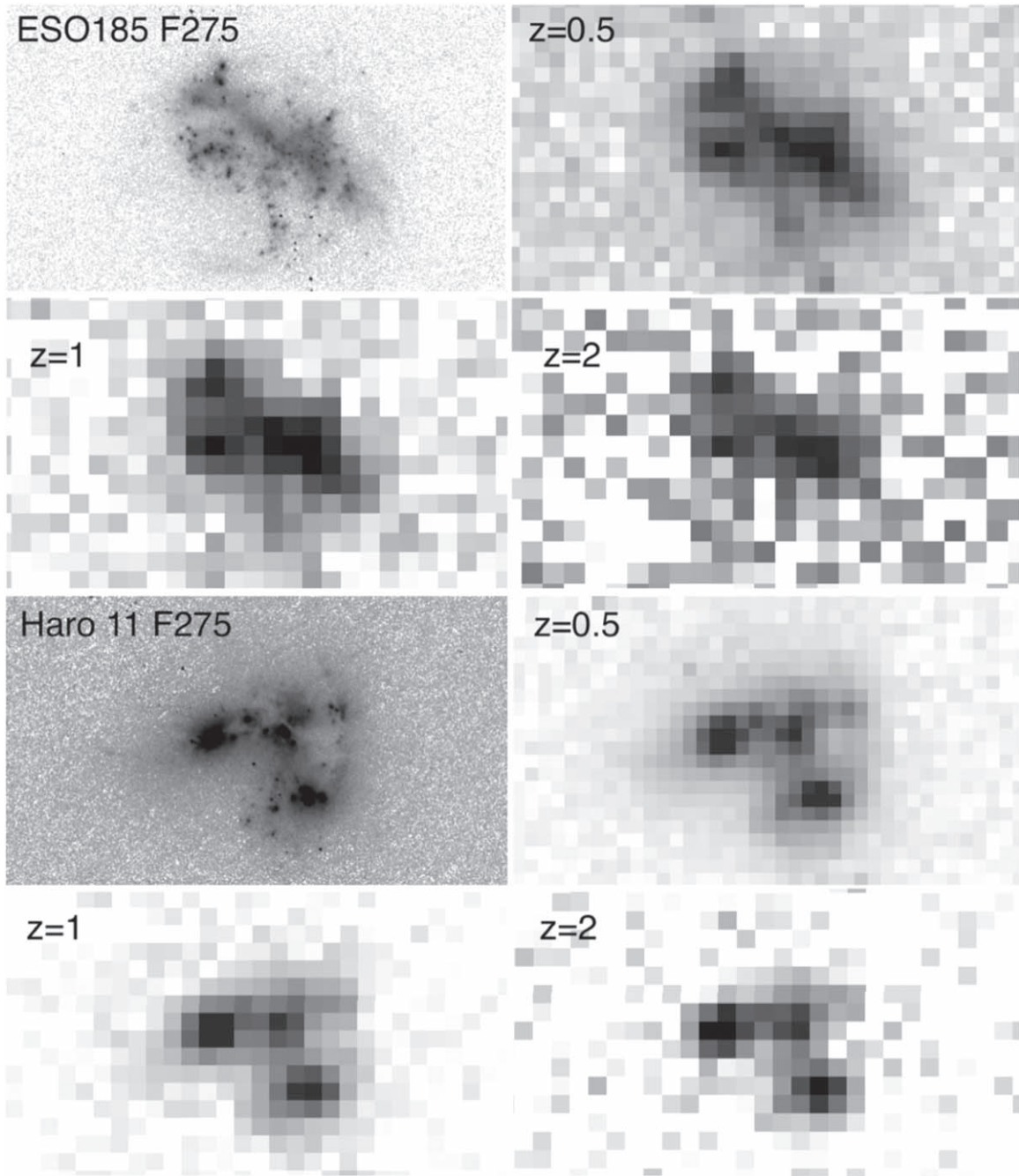


Figure 5. ESO 185 and Haro 11 are shown in filter F275W, and artificially redshifted to $z = 0.5$, 1, and 2 in the panels, as labeled. The spatial size of 1 pixel for redshifts $z = 0.5$, 1, and 2 corresponds to 240 pc, 318 pc, and 335 pc, respectively; the pixel scale of the rest-frame image for each galaxy is given in Table 1. See Figures 1 and 2 for 5 kpc scales. The F275 image artificially redshifted is appropriate for comparison with a $z = 2$ galaxy observed in the R band, a $z = 1$ galaxy observed in the B band, or a $z = 0.5$ galaxy observed in the U band.

trend of younger clumps having a higher Σ . The SFRs as a function of total stellar surface density are shown in the middle panel along with the curve fit. The star formation rate is higher in denser regions. The right panel shows a plot of Σ_{SFR} versus total stellar surface density along with a curve fit, also showing a correlation. The range of Σ_{SFR} for the clumps is consistent with the values for the clumps with high surface density measured by Zaragoza-Cardiel et al. (2018) in their large sample of local interacting galaxies (distances up to 140 Mpc). Figure 4 from Guo et al. (2018) shows a linear fit with a broad spread. Our clumps fall on a line displaced upward from their fit by a factor of ~ 100 , overlapping with the clumps with the

highest star formation rate per unit area in their sample. This is reasonable, since our galaxies are mergers and theirs are typically less extreme interactions.

4.3. Comparison with High- z Clumps

Star-forming clumps in the GEMS, GOODS, and UDF fields were analyzed with the same methods as in this paper, so they allow a direct comparison of their properties. The rest-frame B magnitudes of clumps in interacting galaxies in the GEMS and GOODS fields (Elmegreen et al. 2007a) are very similar to those of local clumps, ranging from -14.5 to -17.5 mag, while

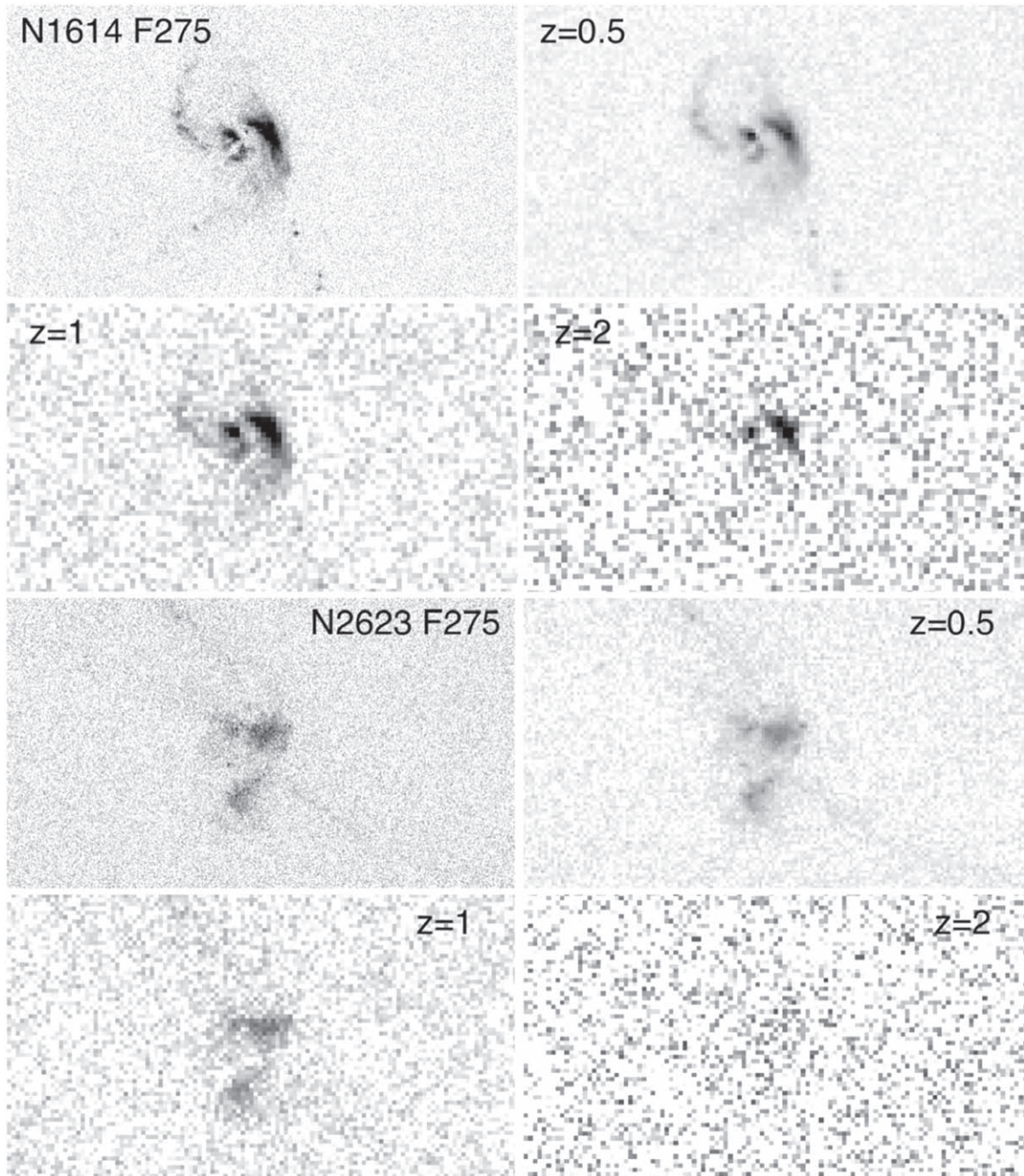


Figure 6. NGC 1614 and NGC 2623 are shown in filter F275W, and artificially redshifted to $z = 0.5, 1$, and 2 in the panels, as labeled. See Figures 2 and 3 for 5 kpc scales.

the rest-frame ($B - V$) colors of clumps in clumpy galaxies studied by Elmegreen et al. (2009b) ranged from -0.8 to 1.8 (the latter corresponding to central bulge-like clumps), with the majority of the clump colors lying between 0 and 1 . Thus, the high- z clumps are very similar to the local clumps in brightness and color.

Clumps in the GEMS and GOODS fields had log ages decreasing from 9 to 8 from redshifts 0.5 to 1.5 , and log masses ranging from about 7 to 8.6 , averaging about 8 across all redshifts from 0.5 to 1.5 (Elmegreen et al. 2009b). The log surface densities in units of $M_{\odot} \text{pc}^{-2}$ of these clumps ranged from about 1.5 to 2 . They were typically 1 kpc in size, which is resolved at these redshifts. For 10 UDF clumpy galaxies from redshifts 1.6 to 3 , the clumps averaged a log mass of

8.75 and log age of 8.4 ; their average log SFR was 0.32 (Elmegreen & Elmegreen 2005), which is essentially the same as the average for the clumps in the present sample. Elmegreen et al. (2009a) considered over 2100 clumps in over 400 chain, clump cluster, and spiral galaxies in the UDF out to redshift $z = 4$. The clumps included star-forming clumps as well as bulge-like clumps; beyond $z = 5$, the masses averaged 10^8 – $10^9 M_{\odot}$. Most galaxies showed no signs of interaction, but a small number showed tidal-like features suggesting mergers.

The diameters of local clumps are similar to those of kiloparsec-size high-redshift clumps in the previously cited samples. The average diameters for the clumps in each galaxy are listed in Table 2.

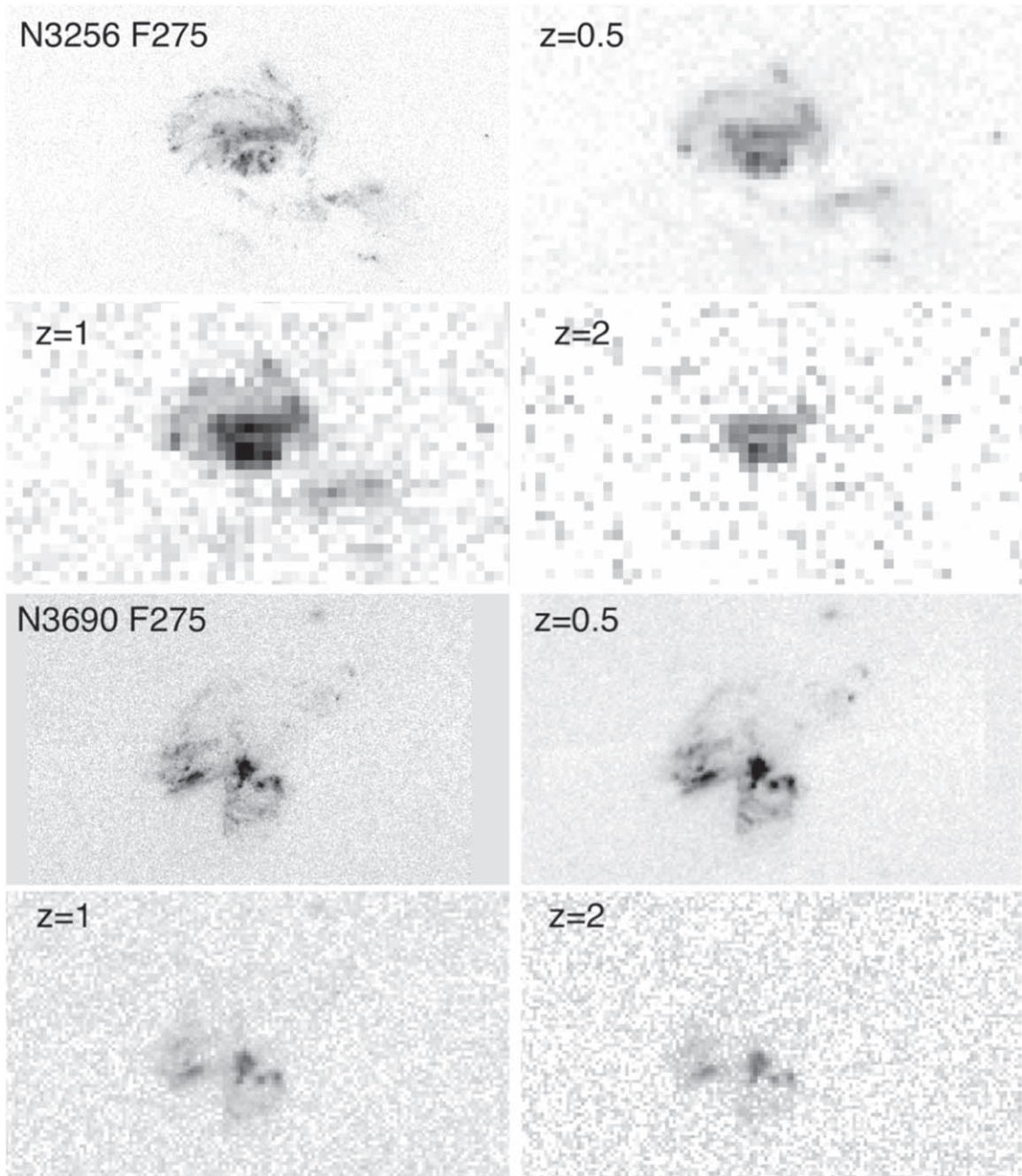


Figure 7. NGC 3256 and NGC 3690 are shown in filter F275W, and artificially redshifted to $z = 0.5$, 1, and 2 in the panels, as labeled. See Figures 3 and 4 for 5 kpc scales.

Dessauges-Zavadsky & Adamo (2018) determined the mass function of 194 clumps in galaxies at redshifts from 1 to 3.5 that are seen in deep HST images. They derived a slope of ~ -1.7 for linear intervals of mass, for $\log \text{mass} > 7.3$. To compare our clumps with theirs, we consider only the 18 clumps of higher mass in our sample, with $\log \text{mass} > 8$. We derive a slope of -1.4 for these clumps, which is similar considering our small sample size.

Clumps in clumpy galaxies in the CANDELS field (Grogan et al. 2011; Koekemoer et al. 2011) were identified by Guo et al. (2015), and their masses were measured by Guo et al. (2018). These studies included nearly 3200 clumps from 1270 galaxies, divided by redshift bins from $z = 0.5$ to 3 and by log

mass of the host galaxy from 9.0 to 11.4. Their Figure 4 shows that the clump masses scale with the galaxy masses, and clumps that had a higher fraction of UV luminosity relative to the galaxy were slightly more massive than less UV-bright clumps. For a given galaxy mass, the results were essentially independent of redshift bin. For galaxy log masses from 9.0 to 9.8, the log masses of UV-bright clumps ranged from about 6.5 to 9.5, with the majority between 8.0 and 8.5. For galaxy log masses from 9.8 to 10.6, the majority of the clump log masses were between 8.6 and 9.4. Less UV-bright clumps were factors of 10–100 times less massive. These results are consistent with the local clumps measured in this paper. Clumps in an additional six galaxies at $z \sim 2$ were studied by Förster

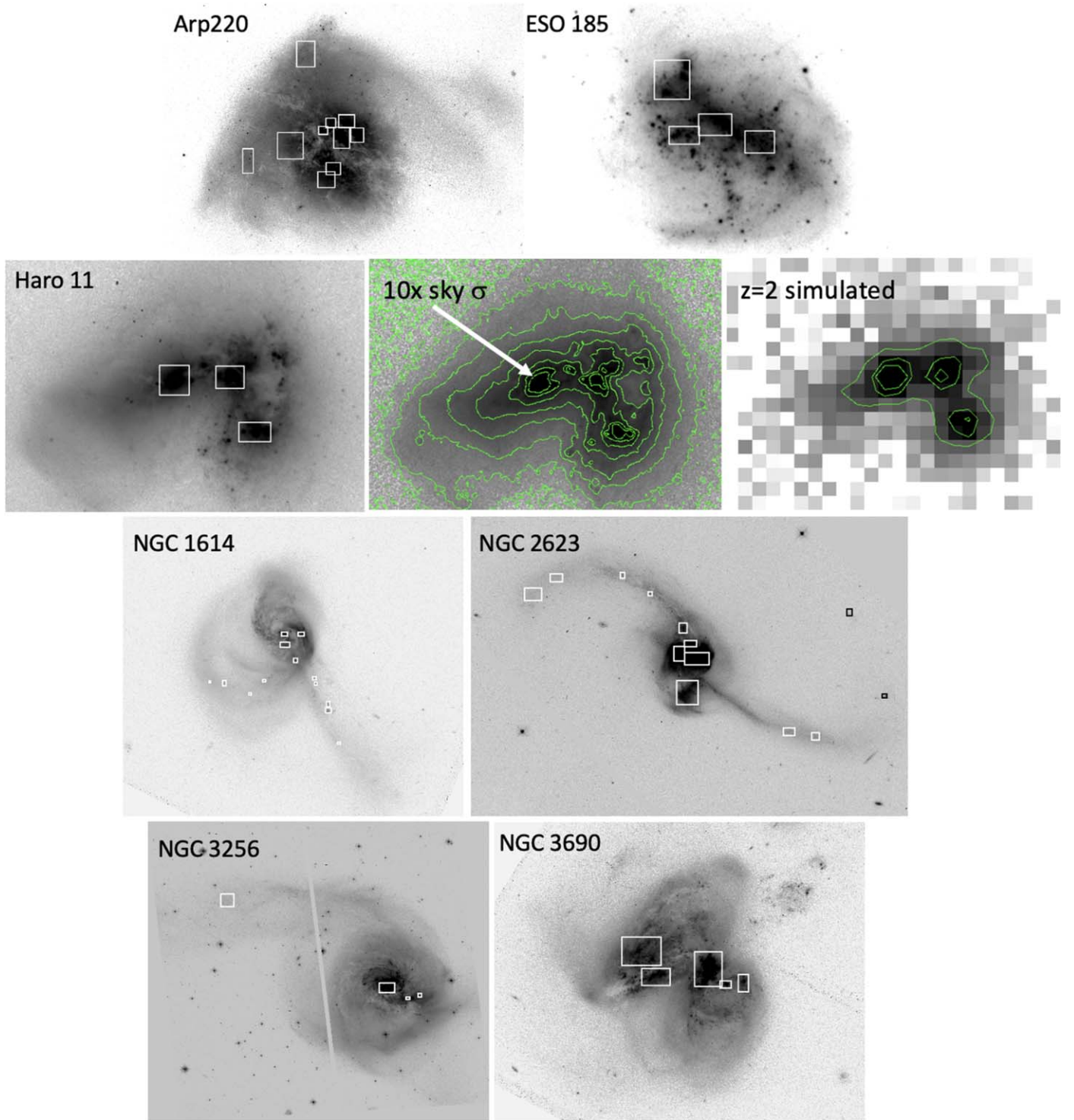


Figure 8. The seven galaxies studied here are shown in the F555W filter. Boxes identify the clumps that were measured; see Figures 1–4 for physical scales. For Haro 11, contour plots are also shown to indicate how clumps were identified. Measurements were done on the non-redshifted images for the boundaries determined from the redshifted images. In practice, these boundaries were at a surface brightness $\sim 10 \times$ sky σ in the F435W image, as indicated in the middle image. The right-hand contour plot is for the simulated $z = 2$ F435W image, where the three clumps are distinct.

Schreiber et al. (2011) with HST infrared images and VLT spectroscopy. They find clump ages ranging from 50 Myr to 2.75 Gyr.

Evidently, the clumps measured in the present study have a range of masses, ages, sizes, star formation rates, and surface densities that are similar to those of high-redshift clumps. This is reasonable, since the turbulent conditions that formed

massive clumps at high z apply also to at least the central regions of local interacting and merging galaxies. Therefore, these local clumps can be used to probe their substructure.

5. Clumps and Star Clusters

A catalog of compact star clusters for the galaxies in our sample was compiled by B. Whitmore et al. (2021, in

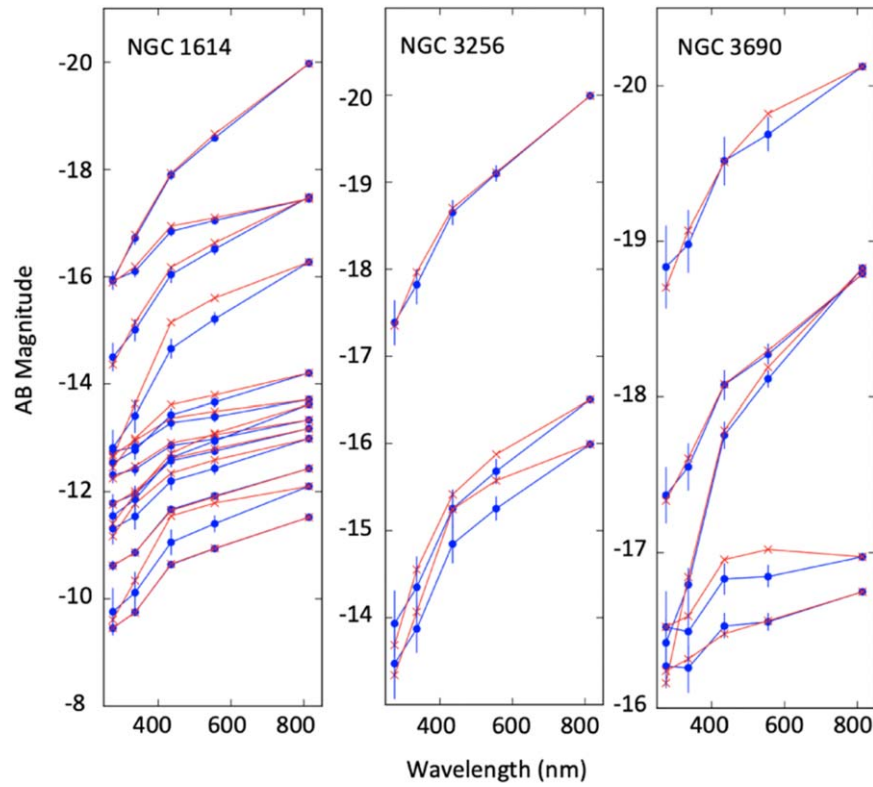


Figure 9. Best fits are shown for the clumps for three of the galaxies in this study, with blue dots showing the models from the SEDs and red crosses for the measurements. Blue vertical lines indicate uncertainties from the model fits. Some of the fainter ones (at the bottom of the figure) are more poorly fit.

Table 2
Average Properties of Clumps

Name	Diameter (kpc)	$\log(\text{mass}/M_{\odot})$	$\log(\text{age}/\text{yr})$	A_V (mag)	$\log(\text{SFR}/M_{\odot} \text{ yr}^{-1})$	Σ ($M_{\odot} \text{ kpc}^{-2}$)	sSFR ($M_{\odot} \text{ yr}^{-1} \text{ kpc}^{-2}$)
Arp 220	1.30 ± 0.45	8.74 ± 0.57	8.90 ± 0.05	2.95 ± 0.90	-0.16 ± 0.61	2.59 ± 0.48	-8.93 ± 0.16
ESO 185	0.60 ± 0.13	7.51 ± 0.37	8.35 ± 0.43	0.52 ± 0.049	-0.84 ± 0.12	2.17 ± 0.23	-8.54 ± 0.34
Haro 11	0.62 ± 0.06	7.73 ± 0.32	7.48 ± 0.19	0.40 ± 0.25	0.24 ± 0.17	2.60 ± 0.31	-7.90 ± 0.24
NGC 1614	0.45 ± 0.17	6.92 ± 1.11	8.26 ± 0.49	1.63 ± 0.83	-1.34 ± 1.3	1.87 ± 0.92	-8.45 ± 0.42
NGC 2623	1.30 ± 0.79	7.44 ± 1.59	8.74 ± 0.42	1.76 ± 1.05	-1.12 ± 1.62	1.44 ± 1.18	-8.65 ± 0.62
NGC 3256	0.75 ± 0.61	8.17 ± 0.71	8.17 ± 0.50	2.06 ± 0.31	1.66 ± 1.31	2.87 ± 0.24	-6.79 ± 0.48
NGC 3690	1.73 ± 0.85	8.13 ± 0.78	7.91 ± 0.51	1.09 ± 0.47	1.88 ± 0.71	2.06 ± 0.29	-6.56 ± 0.29

Note. The average properties of clumps within each galaxy are listed (with the number of clumps listed in Table 1). Mass, age, and extinction are from the SED fits; mass and age refer to the new star formation in the clump. SFR is the young stellar mass divided by the age. Σ is the surface density, from the total mass of the clump including the young and underlying component, divided by the area. sSFR is the specific star formation rate, taken as the SFR divided by the total mass

preparation). The cluster catalogs were constructed using the DAOPHOT software as implemented in IRAF. An aperture radius of 2 pixels was used with a sky annulus between 7 and 9 pixels. A training set of isolated clusters with relatively high signal-to-noise ratio (S/N) was used to determine aperture corrections for the clusters for the F435W, F555W, and F814W filters. In most cases, the S/N for the F336W and F275W filters was too low to be measured directly. In these cases, an offset based on a stellar point-spread function and normalized to the F555W filter was used. In cases where both could be measured, the agreement was roughly 0.2 mag. An example of typical aperture corrections (i.e., for Arp 220) from the aperture of 2 pixels to infinity was 1.097, 0.991, 0.821, 0.741, and 0.913 for F275W, F336W, F435W, F555W, and F814W, respectively.

At the distance of these galaxies, it is difficult to separate stars from clusters based on resolution in most cases. For this reason, normal manual classification techniques are not being

pursued (i.e., unlike for LEGUS (Calzetti et al. 2015) or PHANGS-HST (J. C. Lee et al. 2021, in preparation)). Instead, we are using the fact that the brightest stars generally have $M_V \simeq 9$ (Humphreys & Davidson 1979), and defining anything brighter than this to be a cluster. Objects fainter than this limit are not included in this paper. We will revisit this and related topics in future papers from the CCDG project.

If the local clumps are illustrative of clumps at high redshift, then the clusters inside these local clumps might be illustrative of clusters inside high-redshift galaxies as well. A total of 1596 clusters brighter than $M_V = -9$ are within the clumps. The number of clusters inside clumps in each galaxy is listed in Table 2. Figure 13 shows the local clusters (circles) that are within the clump boundaries (rectangles) on the logarithmic stretches of the F814W images of our galaxies. Arp 220 is anomalous in having very few clusters within the clumps, whereas NGC 3256 and NGC 3690 have hundreds. As the

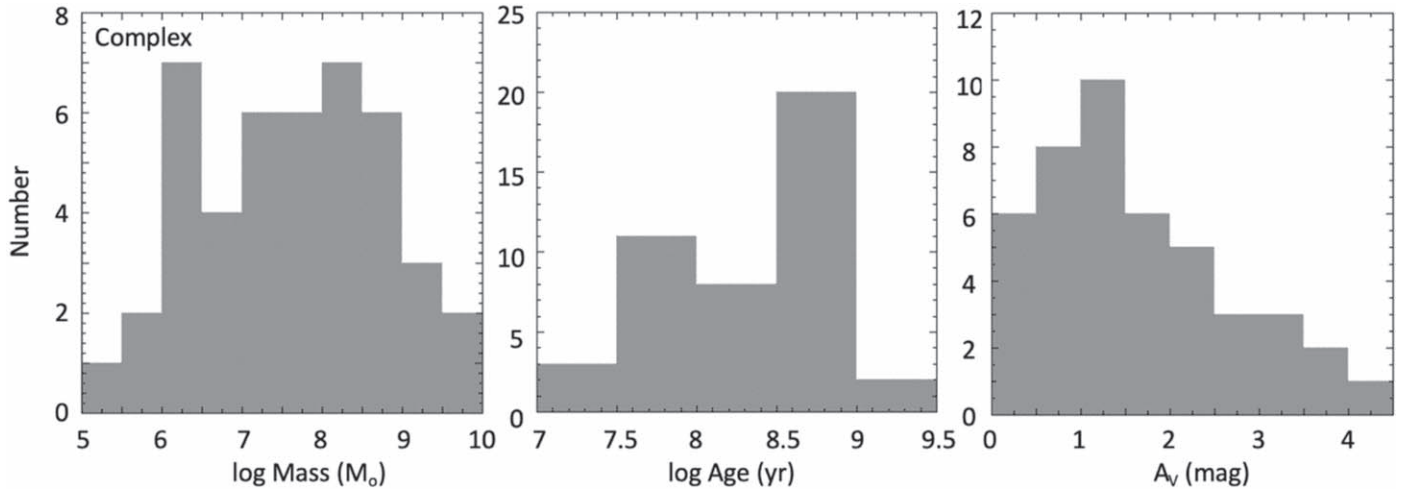


Figure 10. Histograms of the masses, ages, and visual magnitudes of extinction of the clumps from all seven galaxies. The masses are the young star-forming masses, not including the underlying mass of the clump, which would add a factor of ~ 2 more mass.

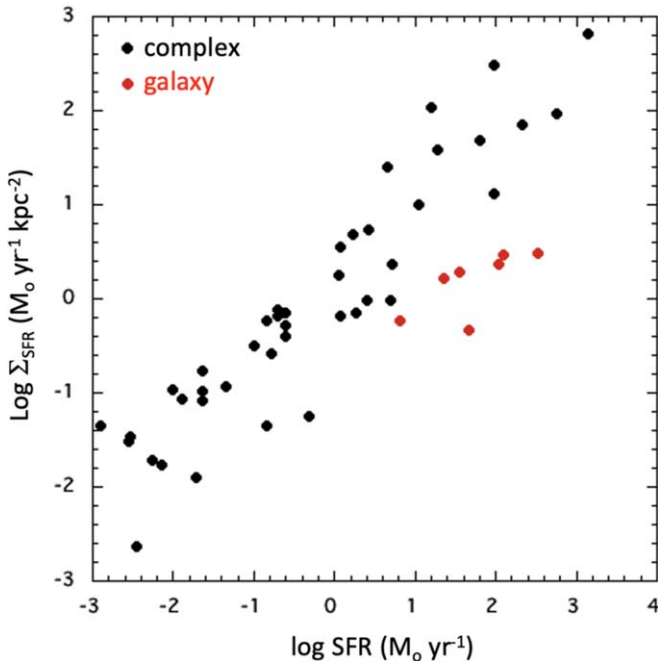


Figure 11. Star formation rate per unit area vs. star formation rate for the clumps (black dots) and their host galaxies (red dots).

figure illustrates, the distributions of clusters within the clumps are fairly uniform, although the concentration of clusters increases in regions within a clump where there are brighter arcs and substructure, such as in NGC 3256 and NGC 3690.

Figure 14 shows a color-color plot of $(U - B)$ versus $(V - I)$ in Vega magnitudes for clusters (black dots) and clumps (red dots) in the four galaxies for which B observations were available: Arp 220, NGC 1614, NGC 3256, and NGC 3690. These are the observed colors, not corrected for extinction; a reddening line is drawn to indicate one magnitude of extinction in the V band. The dark blue line is the evolutionary line from the models of Bruzual & Charlot (2003) for a single burst with solar metallicity, appropriate for comparison with the star clusters. For reference, the light blue line is the evolutionary model for continuous star formation. As described above, the clumps were modeled with a two-component fit using a combination of the continuous and instantaneous models. The

clumps are typically redder than the clusters within them, reflecting the underlying older stars in the clumps. The broad range of colors for the star clusters is consistent with their formation over a wide range of time, rather than in a single burst within the clumps.

The magnitude distribution function for clusters is shown in the left panel of Figure 15, color-coded for each galaxy. Solid lines show the distribution for all the clusters in a given galaxy, while dotted lines show only the clusters that are within clumps in that galaxy.

The clusters inside clumps are brighter than the clusters outside clumps, which is likely a size-of-sample effect (e.g., Whitmore et al. 2007). Overall, the slopes of the distributions look similar from one galaxy to the next, ~ -0.4 on this plot, which has magnitude intervals on the abscissa; this corresponds to a slope of -1 on a similar plot with $\log_{10}(\text{luminosity})$ on the abscissa. In that case the luminosity distribution function in logarithmic intervals is $N(L)d \log L = L^{-\alpha}d \log L$ for $\alpha = 1$. This is equivalent to the typical slope for compact star clusters measured elsewhere (Krumholz & McKee 2019), and is the expected power-law function for clusters in a hierarchical distribution of stellar groupings (Elmegreen & Efremov 1997). The slope is consistent with that for clusters in the Antennae merger (Whitmore et al. 1999, 2010) and for clusters in 22 LIRG galaxies, including some in our sample—NGC 1614, NGC 2623, NGC 3256, and NGC 3690 (Linden et al. 2017). The left panel of Figure 15 also shows that the slopes of the cluster magnitude distributions are about the same for clusters inside and outside clumps, so the clump environment does not affect the slope.

There is a possible but uncertain slight steepening of the slope at the bright end of the cluster distribution function for some of the galaxies. Adamo et al. (2011) found a steepening at the bright end of the cluster function in the dwarf merger galaxy ESO 185-IG13 and suggested steepenings like this in other cluster functions too. However, Mok et al. (2019) found that the cluster mass function in several galaxies, including NGC 3256 (which is in our sample), was well fit by a power law, with no bends or breaks. Mok et al. (2020) used archival CO data from the Atacama Large Millimeter/submillimeter Array (ALMA) to produce a catalog of giant molecular clouds (GMCs) in NGC 3256; the GMCs are spread across its central

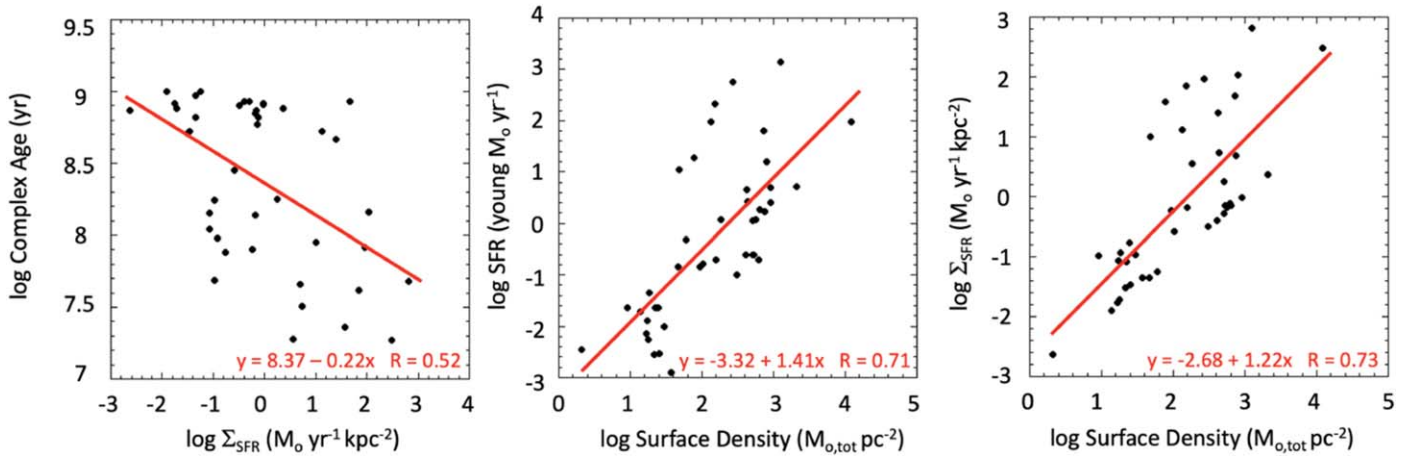


Figure 12. Left: clump age vs. star formation rate per unit area. Middle: clump star formation rate vs. total stellar surface density. Right: clump star formation rate per unit area vs. total stellar surface density.

regions. Both the GMCs and young clusters within them show power-law distributions.

The right-hand panel of Figure 15 plots the magnitude distribution for clusters in two bins of surface brightnesses (red line for brighter and black line for fainter than $19 \text{ mag arcsec}^{-2}$) to examine whether the cluster functions differ between the two cases. Since Arp 220 and NGC 2623 have older clumps than the other galaxies, they were not included in this figure. The other galaxies—ESO 185–IG13, Haro 11, NGC 1614, NGC 3256, and NGC 3690—have clumps spanning a similar range of younger ages so they are combined. The average I -band surface brightness of the clumps in these galaxies is $19 \text{ mag arcsec}^{-2}$. The plot divides clumps into those brighter than average (shown in red) and those fainter than average (shown in black). For each subset, the number of all clusters within all clumps is shown as a function of the absolute magnitude M_V of the cluster. The distributions are very similar for the brighter and fainter clumps, although of course the brighter clumps contain more clusters.

The integrated magnitude for all the clusters in a clump was compared to the magnitude of the clump in different filters. There was wide variation for clumps with a galaxy. Overall, clumps were on average 0.1 mag brighter in the near-UV (NUV) (F275W) than the integrated cluster light for Haro 11, about 1 mag for NGC 1614, NGC 3256, and NGC 3690, 3 mag for ESO 185–IG13 and NGC 2623, and 5 mag for Arp 220. Thus, the clusters contribute about 90%, 40%, 6%, and 1% of the NUV clump light for these galaxies, respectively.

6. Tidal Tails

The galaxies in this sample all show multiple tidal tails, shells, and tidal debris. In what follows, these features are all referred to as “tidal tails,” including well-defined tails such as in NGC 2623 as well as more diffuse tidal debris or shells such as in NGC 3256, just as was done in the GEMS and GOODS study (Elmegreen et al. 2007a). ESO 185–IG13, Haro 11, and NGC 3690 have short tails and NGC 3690 is a mid-stage merger (Linden et al. 2017). NGC 2623 shows two long tails with a few small wisps; it is thought to be in a more advanced merger state (Evans et al. 2008). NGC 2623 was also found to have two intense periods of star formation from less than 140 Myr to 1.4 Gyr ago (Cortijo-Ferrero et al. 2017). Arp 220 has short looping structures and may be a late-stage merger

with counter-rotating nuclei (Barcos-Muñoz et al. 2015). NGC 1614 and NGC 3256 have similar multiple looping structures; NGC 3256 is a late-stage merger (Linden et al. 2017).

In order to compare the tidal tails to those in high-redshift galaxies, we sampled the tails in several different positions to get their average properties. These positions avoided obvious star clusters and clumps. Figure 16 shows boxes for the 81 positions in which surface photometry was done, using the IRAF task *imstat* as was done for the clumps. Table 3 lists the average surface brightnesses and colors of the tidal tails in each galaxy. Both of these quantities are similar in ESO 185 and Haro 11, which are morphologically similar also. NGC 2623 has the arms with the highest surface brightness. The surface brightnesses are similar for Arp 220 and NGC 3690 and for NGC 1614 and NGC 3256. Average values for the features measured in each galaxy are also listed. The average $(V - I)$ color is about 1 mag, and ranges from about 0.5 to 1.5 mag independent of surface brightness.

Mullan et al. (2011) studied tidal tails in a diverse sample of 17 local interacting galaxies with HST observations, using the same method as in this paper to measure several random positions within the tidal arms. There, the V -band tail surface brightnesses averaged $24 \text{ mag arcsec}^{-2}$ and ranged from 22 to $25.5 \text{ mag arcsec}^{-2}$. The average $(V - I)$ color was 1 mag, ranging from 0.6 to 1.4 mag, so their properties are similar to those of the tails and debris in the current sample, although there were not any tails in the Mullan study as bright as the brightest tails here.

The V -band surface brightnesses of the GEMS and GOODS tails (Elmegreen et al. 2007a) compared with the galaxies in this sample are shown in Figure 17 as a function of $\log(1+z)^4$, since cosmological dimming decreases surface brightness by $(1+z)^4$. Thus, there is a drop of 2.5 mag for each drop of 1 unit in $\log(1+z)^4$. For $z = 0.5, 0.8, 1$, and 2 , the corresponding decreases are 1.8, 2.5, 3, and $4.8 \text{ mag arcsec}^{-2}$. The 2σ surface brightness detection is about $24.5 \text{ mag arcsec}^{-2}$ in the GEMS and GOODS fields. For a $z = 0.8$ galaxy, this would correspond to a local tail surface brightness of $22 \text{ mag arcsec}^{-2}$, which is the average value for the local galaxies in this sample. The tails in NGC 2623 and Haro 11 are so bright that they would still be visible at $z = 2$, while all but the brightest patches in Arp 220, NGC 1614, or NGC 3690 would not be observed. Thus, some galaxies beyond $z = 1$ could be mergers that are not obvious from their tidal features.

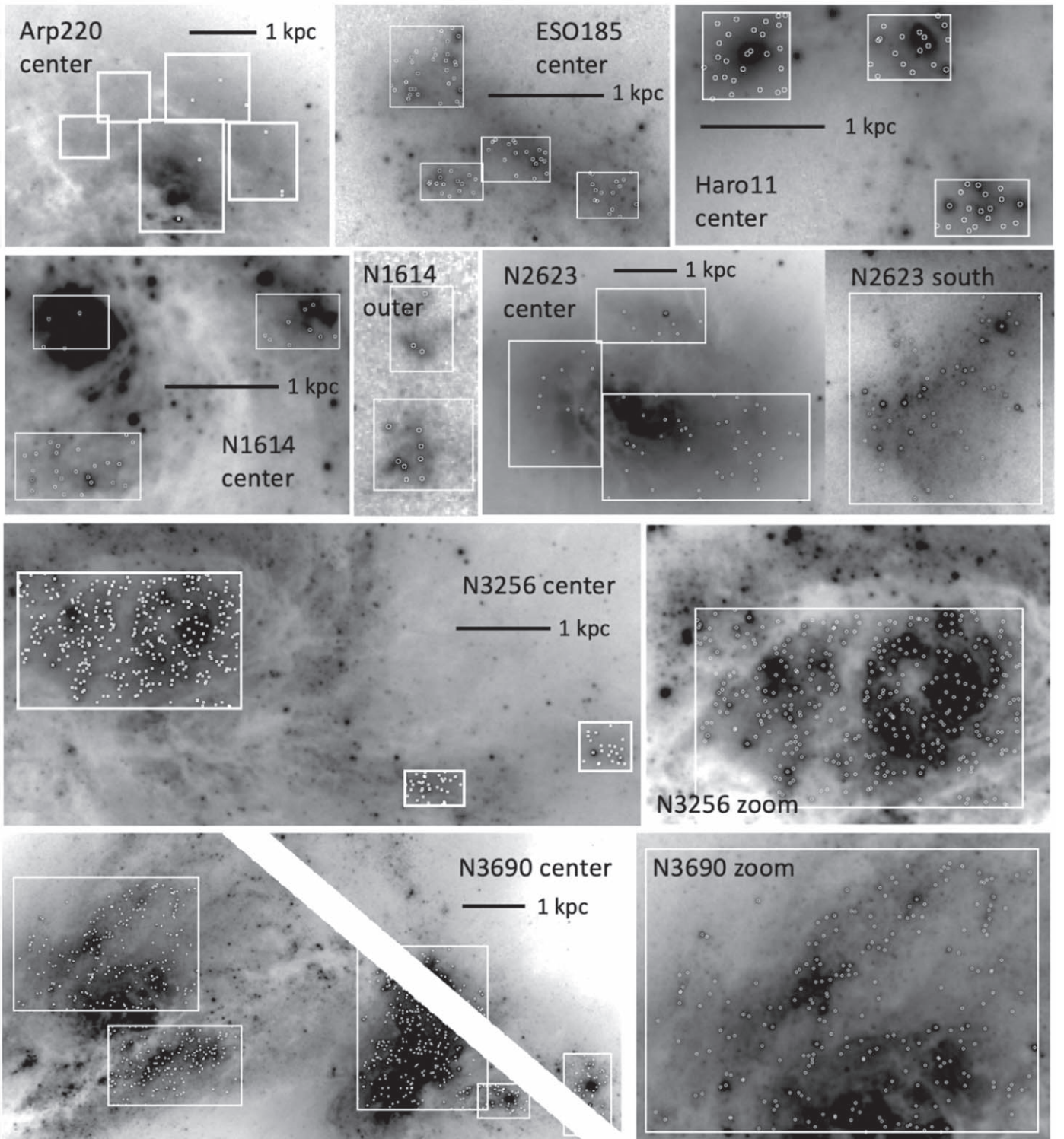


Figure 13. Boxes outline some of the clumps in each galaxy, while open circles indicate the locations of clusters within each clump. The images are logarithmic stretches in the F814W filter. Physical scales of 1 kpc are indicated by a solid black line.

Tidal tails may be observable for only the first few hundred million years in the early stages of a merger because the surface brightness dims as the stars age and disperse (Mihos 1995). Hibbard & Yun (1999) measured the surface brightness of the nearby merger, Arp 299, which has an interaction age of 750 Myr. The faintest tail region they measured goes down to

$28.5 \text{ mag arcsec}^{-2}$ in the B band. This would be undetectable at high z using the limits assumed here.

Our redshifted HST images of local mergers show some large star-forming clumps in the tidal tails. In some galaxies, such clumps may be tidal dwarfs, as studied by Duc et al. (2004), Mirabel et al. (1992), and others, but that does not

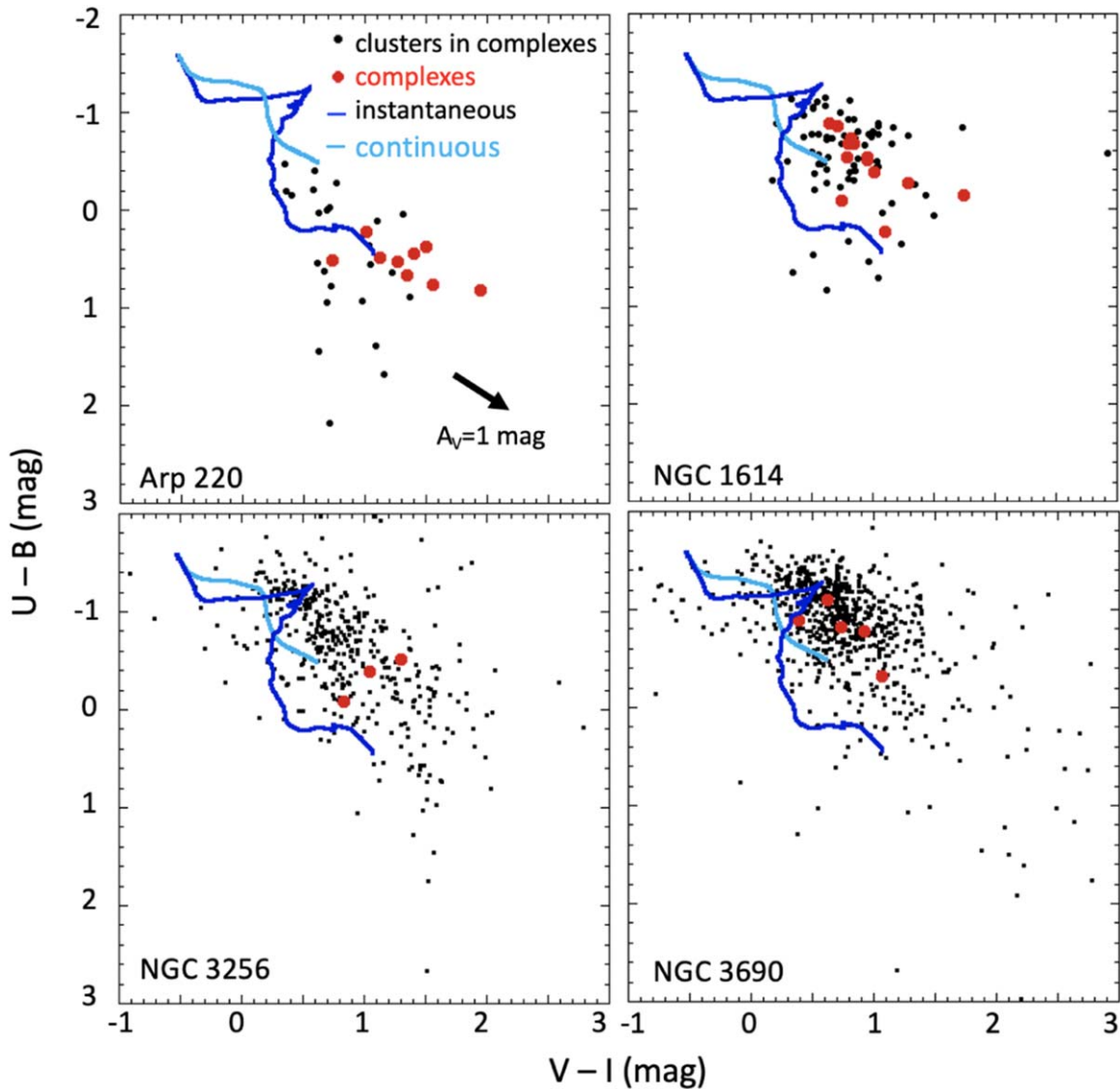


Figure 14. Color-color diagram of $(U - B)$ vs. $(V - I)$ in Vega magnitudes for clusters and clumps in four galaxies. Black dots represent star clusters brighter than $M_V = -9$ that are within a clump, and red dots represent the clumps. These are the observed colors, uncorrected for extinction. Dark blue lines represent the Charlot–Bruzual evolutionary models for solar metallicity, from $\log \text{age} = 5$ in the upper left to 10.3 in the lower right, for instantaneous star formation, so these are appropriate for the clusters. The broad spread of clusters indicates a broad range of ages, consistent with ongoing star formation in the clumps rather than a single burst. The light blue lines represent the Charlot–Bruzual models for continuous star formation, as a guide. The clumps were modeled with a combination of the continuous and instantaneous models, as described in the text.

appear to be the case in the current sample. Similar tidal clumps were discussed for high- z galaxies (Elmegreen et al. 2007a; Zanella et al. 2019).

7. Dust and Gas

7.1. Extinction Minima

Some of the clumps in the local galaxies are outlined by dust extinction, as is evident from the wispy structure occulting the underlying disk in the HST images. The old red clumps in the artificially redshifted image of Arp 220 are of this type, being the inner clear regions of each disk. CO emission in the dusty region between the two bright lobes is seen at low resolution (Scoville et al. 1986; Barcos-Muñoz et al. 2015) and CO emission centered on the optical lobes is seen at high resolution (Brown & Wilson 2019). There are relatively few star clusters in these Arp 220 regions, however, presumably because they

are old, and that also accounts for the interstellar medium clearing around them. Nevertheless a morphology of clumps as artifacts from extinction minima is possible at high redshift too.

Other galaxies in our sample have thin dusty molecular features like Arp 220. NGC 1614 has a thin dust lane cutting across one of the inner clumps next to a broader dust lane, as seen in Figure 6. Its CO emission observed with ALMA is centered on the dust feature and encompasses the western bright regions (König et al. 2016). NGC 3256 also has a dust feature cutting the central region (see Figure 7 and Figure 2 of Zepf et al. 1999), although it does not cut through a clump.

Haro 11, a low-metallicity blue compact dwarf, has no detectable H I or CO, with upper limits of $\sim 10^8 M_\odot$ for each component (Bergvall et al. 2000). Its ionized and diffuse gas component is $5.8 \times 10^8 M_\odot$ based on mid- and far-infrared fine-structure cooling lines observed with the Spitzer Infrared Spectrograph and Herschel Photodetector Array Camera and

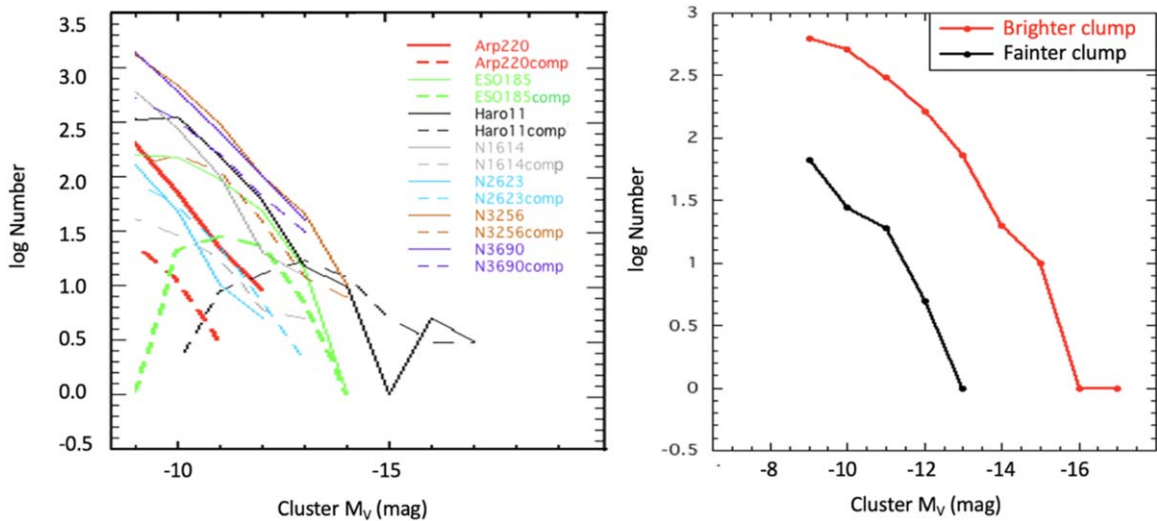


Figure 15. Left: histogram showing the log of the number of clusters as a function of cluster absolute magnitude M_V color-coded by the seven galaxies. Solid lines are for all the clusters in a galaxy, while dotted lines are only for clusters that are in clumps. The distributions all have about the same slope. Right: clumps in galaxies ESO 185, Haro 11, NGC 1614, NGC 3256, and NGC 3690, which all span similar ages, are divided into brighter (red line) and fainter (black line) surface brightnesses, with the midpoint being $19 \text{ mag arcsec}^{-2}$ in the I band. The log of the number of clusters within the clumps is shown vs. the cluster absolute V magnitude. The distributions have the same power-law slope.

Spectrometer by Cormier et al. (2012), who describe the photodissociation region and compact H II regions associated with the three main clumps.

NGC 2623 shows CO emission extended across the central region (Brown & Wilson 2019). It has a dust feature cutting across the middle clump, as is evident particularly in the F275W image of Figure 5 (see also Adamo et al. 2010) but the clump still appears as a single clump when artificially redshifted.

Some bright regions at high redshift could be extinction minima too, appearing as clumps because dust obscures other parts of the extended emission. Tacconi et al. (2008) observed a large CO cloud between the visible star-forming clumps in the submillimeter galaxy N2850.4 at $z = 2.39$, suggesting that the bright clumps are not associated with the densest gas in that case.

These observations suggest that some apparent clumps viewed at high redshift could be only extinction minima, but this is actually rare in our redshifted local sample. Only Arp 220 shows clear evidence for it, and what appears through the extinction is not a star-forming region but two old inner disks of the colliding galaxies.

7.2. Gas Similarities

Local mergers can also be gas-rich with high surface densities, like high-redshift disk galaxies. In our sample, a molecular gas mass of $10^{10} M_\odot$ has been detected in the central region of Arp 220 (Scoville et al. 1986) at high density (Brown & Wilson 2019), with gas surface densities of $(2.2\text{--}4.5) \times 10^5 M_\odot \text{pc}^{-2}$ (Barcos-Muñoz et al. 2015). NGC 3256 has a molecular nuclear disk with a gas density $> 10^3 M_\odot \text{pc}^{-2}$ (Sakamoto et al. 2014), with HCN and HCO^+ outflows (Michiyama et al. 2018). Dense gas tracer isotopes of CO and CN were detected in NGC 1614 (König et al. 2016), isotopes of CO in NGC 2623 (Brown & Wilson 2019), and HCO^+ , HCN, and other dense gas tracers in NGC 3690 (Jiang et al. 2011). CO has been detected with comparable surface densities ($> 500\text{--}700 M_\odot \text{pc}^{-2}$) in $z \sim 2$ galaxies by Tacconi et al. (2008, 2010) and others. For the local mergers, the high gas surface density is the result of in-plane accretion, tidal

compression, and fast compressive turbulence (Renaud et al. 2014). For high-redshift disks, the high gas surface density is presumably from a combination of a large accretion flux continuously processed into stars (Bouché et al. 2010), plus occasional mergers (Conselice 2014; Inoue et al. 2016).

Local mergers and high- z disks also have high gas velocity dispersions. For example, high CO velocity dispersions with no ordered rotation suggest mergers in four $z \sim 2$ submillimeter galaxies (Tacconi et al. 2008), and high $\text{H}\alpha$ dispersions suggest mergers in two UV-bright galaxies (Förster Schreiber et al. 2006). Local interacting galaxies can have high gas velocity dispersions also, such as 50 km s^{-1} FWHM or more in H I (Kaufman et al. 1997, 2012), and local mergers have high gas dispersions too, such as Arp 220 at 300 km s^{-1} (Scoville et al. 1986).

8. Conclusions

HST images of seven strongly interacting and merging disk galaxies in the local universe observed in the CCDG sample have been blurred, dimmed, and re-pixelated to match the observing conditions at high redshift. With these changes, the local galaxies appear similar to high-redshift star-forming galaxies: both are clumpy, and the clumps have about the same range of physical size, mass, intrinsic surface brightness, age, and star formation rate at low and high redshift. This is in contrast to clumps in local non-interacting galaxies, which are smaller and less massive than high-redshift clumps. The observed clumps also have the same range of surface density, star formation per unit area, and specific star formation rate as high-redshift clumps.

These similarities, combined with the loss due to cosmological dimming at high redshift of low-surface-brightness features seen in the local galaxies, such as tidal tails, suggest that some clumpy high- z galaxies that look isolated could really be mergers. Other ambiguities about the characteristics of mergers were discussed in the introduction.

We also studied cataloged star clusters in the local galaxies and found that the clumps contain star clusters with normal luminosity functions. We infer from this that high-redshift

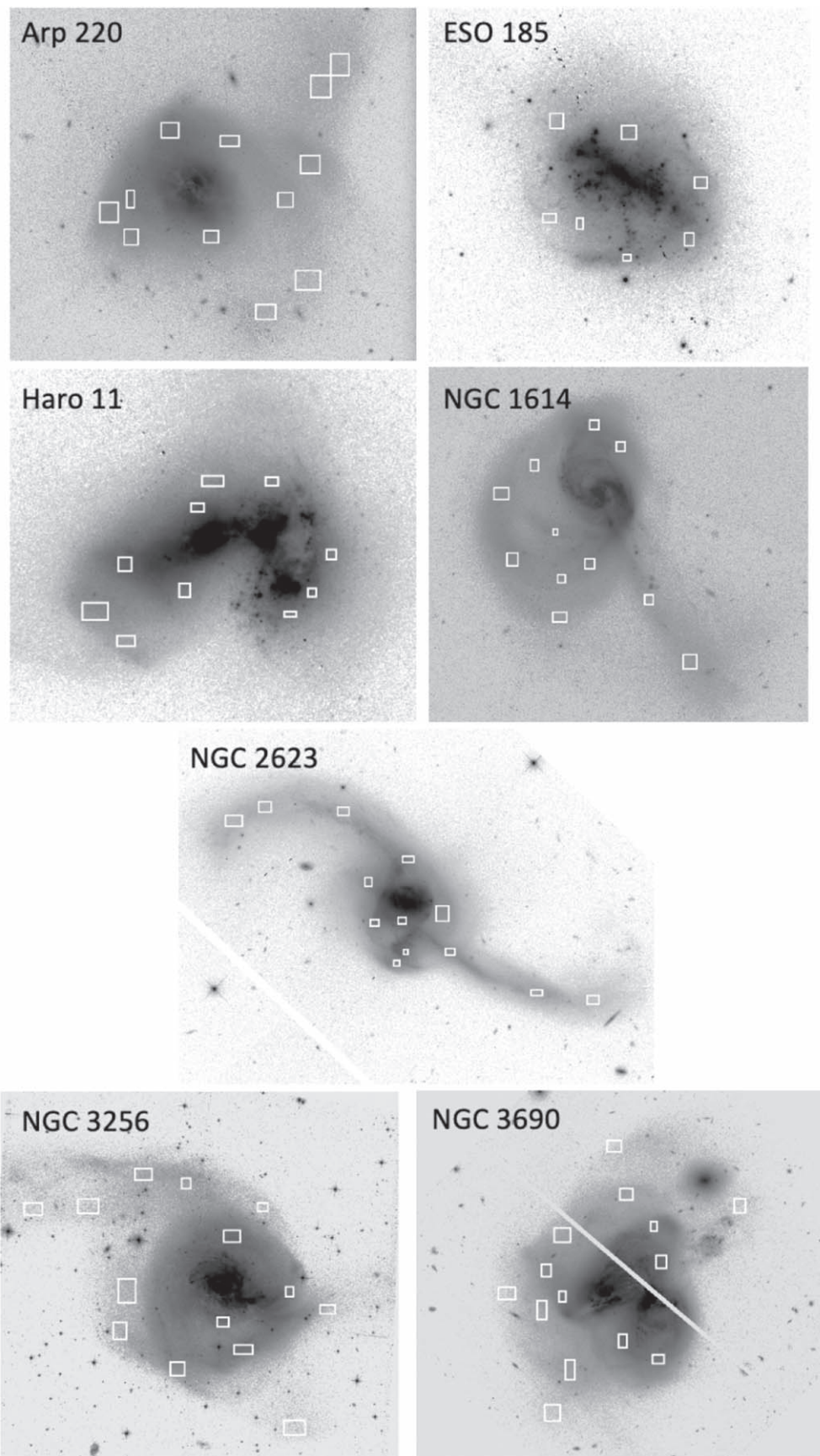


Figure 16. Tail locations where surface photometry was done are indicated by boxes on the logarithmic stretches of the F814W images for each galaxy. See Figures 1–4 for physical scales.

Table 3
Tail Properties

Galaxy	NUV (mag arcsec ⁻²)	<i>U</i> (mag arcsec ⁻²)	<i>B</i> (mag arcsec ⁻²)	<i>V</i> (mag arcsec ⁻²)	<i>I</i> (mag arcsec ⁻²)	NUV – <i>U</i> (mag)	<i>U</i> – <i>B</i> (mag)	<i>B</i> – <i>V</i> (mag)	<i>V</i> – <i>I</i> (mag)
Arp 220	25.35 ± 1.64	24.25 ± 0.98	23.56 ± 0.91	23.2 ± 1.07	21.92 ± 0.96	1.27 ± 1.82	0.69 ± 0.24	0.36 ± 0.18	1.27 ± 0.14
ESO 185–IG13	21.84 ± 0.65	...	22.00 ± 0.54	21.57 ± 0.48	20.92 ± 0.51	0.42 ± 0.07	0.65 ± 0.54
Haro 11	21.23 ± 1.34	...	21.27 ± 0.69	20.84 ± 0.66	20.12 ± 0.54	0.43 ± 0.06	0.73 ± 0.21
NGC 1614	25.19 ± 0.59	23.62 ± 0.56	23.48 ± 0.62	22.84 ± 0.61	21.66 ± 0.62	1.98 ± 0.54	0.15 ± 0.16	0.63 ± 0.09	1.18 ± 0.07
NGC 2623	22.11 ± 1.10	...	20.84 ± 0.63	20.33 ± 0.67	19.40 ± 0.72	0.52 ± 0.08	0.93 ± 0.09
NGC 3256	24.94 ± 1.49	24.84 ± 1.72	24.28 ± 1.28	23.22 ± 1.12	22.71 ± 1.64	1.04 ± 1.49	0.80 ± 1.08	1.18 ± 0.70	0.51 ± 0.60
NGC 3690	24.51 ± 0.99	24.04 ± 1.52	24.02 ± 1.46	23.29 ± 1.47	22.62 ± 1.65	0.79 ± 0.64	0.00 ± 0.31	0.44 ± 0.52	1.29 ± 0.25
Average	23.50 ± 2.02	24.19 ± 1.31	22.94 ± 1.67	22.24 ± 1.51	21.43 ± 1.63	1.19 ± 1.32	0.42 ± 0.65	0.61 ± 0.47	0.94 ± 0.41

Note. The table lists the average surface brightnesses or colors (for the number of tail measurements listed in Table 1) for the different filters: NUV is F275W, *U* is F336W, *B* is either F435W or F438W, *V* is F555W, and *I* is F814W.

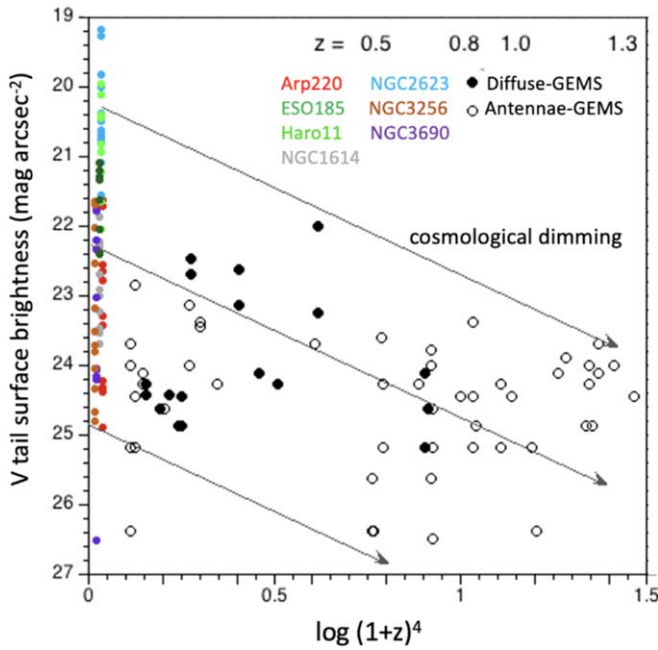


Figure 17. V-band tail surface brightness is plotted as a function of $\log(1+z)^4$. Corresponding redshifts, z , are indicated along the top x-axis. Measurements of tails from the local merger sample are labeled. Tails from GEMS and GOODS galaxies (Elmegreen et al. 2007a) are marked as diffuse (closed circles) or antennae (open circles); for compactness in the legend, those labeled as GEMS also include GOODS galaxies. The latter used F606W, instead of F555W used in the present sample. The lines indicate cosmological dimming.

clumps contain (unresolved) normal bound clusters also, as a consequence of a hierarchy of star formation.

We thank the referee for helpful suggestions to improve the paper. Based on observations with the NASA/ESA Hubble Space Telescope, obtained at the Space Telescope Science Institute, which is operated by the Association of Universities for Research in Astronomy, Incorporated, under NASA contract NAS5-26555. Support for program number HST-GO-15649 was provided through a grant from the STScI under NASA contract NAS5-26555. This research has made use of the NASA/IPAC Extragalactic Database (NED), which is operated by the Jet Propulsion Laboratory, California Institute of Technology, under contract with the National Aeronautics and Space Administration.

ORCID iDs

Debra Meloy Elmegreen <https://orcid.org/0000-0002-1392-3520>
 Bruce G. Elmegreen <https://orcid.org/0000-0002-1723-6330>
 Bradley C. Whitmore <https://orcid.org/0000-0002-3784-7032>
 Rupali Chandar <https://orcid.org/0000-0003-0085-4623>
 Daniela Calzetti <https://orcid.org/0000-0002-5189-8004>
 Janice C. Lee <https://orcid.org/0000-0002-2278-9407>
 Richard White <https://orcid.org/0000-0002-9194-2807>
 David Cook <https://orcid.org/0000-0002-6877-7655>
 Angus Mok <https://orcid.org/0000-0001-7413-7534>
 Sean T. Linden <https://orcid.org/0000-0002-1000-6081>

References

Adamo, A., Hollyhead, K., Messa, M., et al. 2020, *MNRAS*, 499, 3267
 Adamo, A., Östlin, G., Zackrisson, E., et al. 2010, *MNRAS*, 407, 870

Adamo, A., Östlin, G., Zackrisson, E., & Hayes, M. 2011, *MNRAS*, 414, 1793
 Barcos-Muñoz, L., Leroy, A. K., Evans, A. S., et al. 2015, *ApJ*, 799, 10
 Bergvall, N., Masegosa, J., Östlin, G., & Cernicharo, J. 2000, *A&A*, 359, 41
 Blumenthal, K. A., Moreno, J., Barnes, J. E., et al. 2020, *MNRAS*, 492, 2075
 Bouché, N., Dekel, A., Genzel, R., et al. 2010, *ApJ*, 718, 1001
 Brown, T., & Wilson, C. D. 2019, *ApJ*, 819, 17
 Bruzual, G., & Charlot, S. 2003, *MNRAS*, 344, 1000
 Calzetti, D., Lee, J. C., Sabbi, E., et al. 2015, *AJ*, 149, 51
 Cava, A., Schaerer, D., Richard, J., et al. 2017, *NatAs*, 2, 76
 Chandar, R. 2018, HST Proposal, Cycle 26, ID., #15649
 Cibinel, A., Daddi, E., Sargent, M. T., et al. 2019, *MNRAS*, 485, 5631
 Conselice, C. J. 2014, *ARA&A*, 52, 291
 Cormier, D., LeBouteiller, V., Madden, S. C., et al. 2012, *A&A*, 548, A20
 Cortijo-Ferrero, C., González Delgado, R. M., Pérez, E., Fernandes, Cid., & García-Benito, R. 2017, *A&A*, 607, A70
 Cowie, L., Hu, E., & Songaila, A. 1995, *AJ*, 110, 1576
 Davé, R., Anglés-Alcázar, D., Narayanan, D., et al. 2019, *MNRAS*, 486, 2827
 Davé, R., Crain, R. A., Stevens, A. R. H., et al. 2020, *MNRAS*, 497, 146
 Dessauges-Zavadsky, M., & Adamo, A. 2018, *MNRAS*, 479L, 118
 Duc, P.-A., Bournaud, F., & Masset, F. 2004, *A&A*, 427, 803
 Duncan, K., Conselice, C. J., Mundy, C., et al. 2019, *ApJ*, 876, 110
 Elmegreen, B. G., & Efremov, Y. N. 1997, *ApJ*, 480, 235
 Elmegreen, B. G., & Elmegreen, D. M. 2005, *ApJ*, 627, 632
 Elmegreen, B. G., Elmegreen, D. M., Fernandez, M. X., & Lemonias, J. J. 2009a, *ApJ*, 692, 12
 Elmegreen, D. M., & Elmegreen, B. G. 2006, *ApJ*, 651, 676
 Elmegreen, D. M., Elmegreen, B. G., Ferguson, T., & Mullan, B. 2007a, *ApJ*, 663, 734
 Elmegreen, D. M., Elmegreen, B. G., Marcus, M. T., et al. 2009b, *ApJ*, 701, 306
 Elmegreen, D. M., Elmegreen, B. G., Ravindranath, S., & Coe, D. 2007b, *ApJ*, 658, 763
 Evans, A. S., Vavilkin, T., Pizagno, J., et al. 2008, *ApJL*, 675, L69
 Fensch, J., Renaud, F., Bournaud, F., et al. 2017, *MNRAS*, 465, 1934
 Ferreira, L., Conselice, C., Duncan, K., et al. 2020, *ApJ*, 895, 115
 Förster Schreiber, N., Genzel, R., Lehnert, N., et al. 2006, *ApJ*, 645, 1062
 Förster Schreiber, N., Shapley, A. E., Genzel, R., et al. 2011, *ApJ*, 739, 45
 Giallisco, M., Ferguson, H., Koekemoer, A., et al. 2004, *ApJL*, 600, L103
 Grogin, N., Kocevski, D., Faber, S., et al. 2011, *ApJS*, 197, 35
 Guo, Y., Ferguson, H., Bell, E., et al. 2015, *ApJ*, 800, 39
 Guo, Y., Rafelski, M., Bell, E., et al. 2018, *ApJ*, 853, 108
 Hibbard, J. E., & Yun, M. S. 1999, *AJ*, 118, 162
 Hopkins, P. F., Croton, D., & Bundy, K. 2010, *ApJ*, 724, 915
 Humpreys, R. M., & Davidson, K. 1979, *ApJ*, 232, 409
 Hung, C.-L., Hayward, C. C., Smith, H. A., et al. 2016, *ApJ*, 816, 99
 Inoue, S., Dekel, A., Mandelker, N., et al. 2016, *MNRAS*, 456, 2052
 Jiang, X., Wang, J., & Gu, Q. 2011, *MNRAS*, 418, 1753
 Kaufman, M., Brinks, E., Elmegreen, D. M., et al. 1997, *AJ*, 114, 2323
 Kaufman, M., Grupe, D., Elmegreen, B. G., et al. 2012, *AJ*, 144, 156
 Knapen, J. H., Cisternas, M., & Querejeta, M. 2015, *MNRAS*, 454, 1742
 Koekemoer, A., Faber, S., Ferguson, H., et al. 2011, *ApJS*, 197, 36
 König, S., Aalto, S., Müller, S., et al. 2016, *A&A*, 594, A70
 Krumholz, M. R., & McKee, C. F. 2019, *ARA&A*, 57, 227
 Larson, K. L., Díaz-Santos, T., Armus, L., et al. 2020, *ApJ*, 888, 92
 Linden, S. T., Evans, A. S., Rich, J., et al. 2017, *ApJ*, 843, 91
 Mantha, K. B., McIntosh, D. H., Brennan, R., et al. 2018, *MNRAS*, 475, 1549
 Martin, G., Kaviraj, S., Devriendt, J. E. G., et al. 2017, *MNRAS*, 472L, 50
 Menacho, V., Östlin, G., Bik, A., et al. 2019, *MNRAS*, 487, 3183
 Michiyama, T., Iono, D., Sliwa, K., et al. 2018, *ApJ*, 868, 95
 Mihos, C. 1995, *ApJL*, 438, L75
 Mirabel, I. F., Dottori, H., & Lutz, D. 1992, *A&A*, 256, L19
 Mok, A., Chandar, R., & Fall, S. M. 2019, *ApJ*, 872, 93
 Mok, A., Chandar, R., & Fall, S. M. 2020, *ApJ*, 893, 135
 Mullan, B., Konstantopoulos, I. S., Kepley, A. A., et al. 2011, *ApJ*, 731, 93
 Mundy, C. J., Conselice, C. J., Duncan, K. J., et al. 2017, *MNRAS*, 470, 3507
 O’Leary, J. A., Moster, B. P., Naab, T., & Somerville, R. S. 2021, *MNRAS*, 501, 3215
 Pearson, W. J., Wang, L., Alpaslan, M., et al. 2019, *A&A*, 631A, 51
 Pillepich, A., Springel, V., Nelson, D., et al. 2018, *MNRAS*, 473, 4077
 Renaud, F., Bournaud, F., Kraljic, K., & Duc, P.-A. 2014, *MNRAS*, 442L, 33
 Ribeiro, B., Le Fèvre, O., Cassata, P., et al. 2017, *A&A*, 608A, 16
 Rix, H.-W., Barden, M., Beckwith, S., et al. 2004, *ApJS*, 152, 163
 Sakamoto, K., Aalto, S., Combes, F., Evans, A., & Peck, A. 2014, *ApJ*, 797, 90

- Sánchez Almeida, J., Elmegreen, B. G., Muñoz-Tuñón, C., & Elmegreen, D. M. 2014, [A&ARv](#), **22**, 71
- Sancisi, R., Fraternali, F., Oosterloo, T., & van der Hulst, T. 2008, [A&ARv](#), **15**, 189
- Sanders, D. B., & Mirabel, I. F. 1996, [ARA&A](#), **34**, 749
- Schaye, J., Crain, R. A., Bower, R. G., et al. 2015, [MNRAS](#), **446**, 521
- Scoville, N. Z., Sanders, D. B., Sargent, A. I., et al. 1986, [ApJL](#), **311**, L47
- Simons, R. C., Kassin, S. A., Snyder, G. F., et al. 2019, [ApJ](#), **874**, 59
- Simons, R. C., Kassin, S. A., Weiner, B. J., et al. 2017, [ApJ](#), **843**, 46
- Snyder, G. F., Lotz, J. M., Rodriguez-Gomez, V., et al. 2017, [MNRAS](#), **468**, 207
- Spergel, D., Verde, L., Peiris, H. V., et al. 2003, [ApJS](#), **148**, 175
- Tacconi, L. J., Genzel, R., Lutz, D., et al. 2002, [ApJ](#), **580**, 73
- Tacconi, L. J., Genzel, R., Neri, R., et al. 2010, [Natur](#), **463**, 781
- Tacconi, L. J., Genzel, R., Smail, I., et al. 2008, [ApJ](#), **680**, 246
- van den Bergh, S., Abraham, R. G., Ellis, R. S., et al. 1996, [AJ](#), **112**, 359
- Ventou, E., Contini, T., Bouché, N., et al. 2019, [A&A](#), **631A**, 87
- Vivian, U., Sanders, D. B., Mazzarella, J. M., et al. 2012, [ApJS](#), **203**, 9
- Wen, Z. Z., & Zheng, X. Z. 2016, [ApJ](#), **832**, 90
- Wheeler, J., Glenn, J., Rangwala, N., & Fyhrie, A. 2020, [ApJ](#), **896**, 43
- Whitmore, B., Chandar, R., & Fall, M. 2007, [AJ](#), **133**, 1067
- Whitmore, B., Chandar, R., Schweizer, F., et al. 2010, [AJ](#), **140**, 75
- Whitmore, B., Zhang, Q., Leitherer, C., et al. 1999, [AJ](#), **118**, 1551
- Wilson, T. J., Shapley, A. E., Sanders, R. L., et al. 2019, [ApJ](#), **874**, 18
- Wisnioski, E., Förster Schreiber, N. M., Fossati, M., et al. 2019, [ApJ](#), **886**, 124
- Wisnioski, E., Förster Schreiber, N. M., Wuyts, S., et al. 2015, [ApJ](#), **799**, 209
- Xu, K., Liu, C., Jing, Y., Wang, Y., & Lu, S. 2020, [ApJ](#), **895**, 100
- Zanella, A., Le Floch, E., Harrison, C. M., et al. 2019, [MNRAS](#), **489**, 2792
- Zaragoza-Cardiel, J., Smith, B. J., Rosado, M., et al. 2018, [ApJS](#), **234**, 35
- Zepf, S. E., Ashman, K. M., English, J., Freeman, K. C., & Sharples, R. M. 1999, [AJ](#), **118**, 752